Sensing of cytoplasmic chromatin by cGAS activates innate immune response in SARS-CoV-2 infection

Zhuo Zhou
School of Life Sciences, Peking University
Xinyi Zhang
Peking University https://orcid.org/0000-0002-9972-3115
Xiaobo Lei
Peking University
Xia Xiao
Chinese Academy of Medical Sciences
Tao Jiao
Institute of Pathogen Biology, Chinese Academy of Medical Sciences and Peking Union Medical College
Ruiyi Ma
Chinese Academy of Medical Sciences
Xiaojing Dong
Chinese Academy of Medical Sciences
Qi Jiang
Chinese Academy of Medical Sciences and Peking Union Medical College
Wenjing Wang
Chinese Academy of Medical Sciences
Yujin Shi
Chinese Academy of Medical Sciences and Peking Union Medical College
Tian Zheng
Sun Yat-sen University
Yuting Tan
Harvard Medical School
Zichun Xiang
Chinese Academy of Medical Sciences
Lili Ren
Chinese Academy of Medical Sciences and Peking Union Medical College
Tao Deng
Institute of Microbiology, Chinese Academy of Sciences
Zhengfan Jiang

Peking University https://orcid.org/0000-0002-1247-1382

Zhixun Dou

Massachusetts General Hospital https://orcid.org/0000-0002-3069-3907

Wensheng Wei

Peking University https://orcid.org/0000-0002-8053-2423

Jianwei Wang (jianwei.wang@ipbcams.ac.cn)

Chinese Academy of Medical Sciences and Peking Union Medical College https://orcid.org/0000-0002-1116-4559

Article

Keywords: SARS-CoV-2, COVID-19, immune response

Posted Date: February 23rd, 2021

DOI: https://doi.org/10.21203/rs.3.rs-235742/v1

Sensing of cytoplasmic chromatin by cGAS activates innate immune response in SARS-CoV-2 infection

Zhuo Zhou[1,8]*, Xinyi Zhang[1]*, Xiaobo Lei[2,3,4]*, Xia Xiao[2]*, Tao Jiao[2], Ruiyi Ma[2], Xiaojing Dong[2], Qi Jiang[2], Wenjing Wang[2], Yujin Shi[2], Tian Zheng[2], Yuting Tan[5], Zichun Xiang[2,3,4], Lili Ren[2,3,4], Tao Deng[6], Zhengfan Jiang[7], Zhixun Dou[5], Wensheng Wei[1,8], Jianwei Wang[2,3,4,8]

[1]Biomedical Pioneering Innovation Center, Beijing Advanced Innovation Center for Genomics, Peking-Tsinghua Center for Life Sciences, Peking University Genome Editing Research Center, State Key Laboratory of Protein and Plant Gene Research, School of Life Sciences, Peking University, Beijing, China.

[2]NHC Key Laboratory of System Biology of Pathogens, Institute of Pathogen Biology, Chinese Academy of Medical Sciences and Peking Union Medical College, 100730 Beijing, P.R. China.

[3]Key Laboratory of Respiratory Disease Pathogenomics, Chinese Academy of Medical Sciences and Peking Union Medical College, 100730 Beijing, P.R. China.

[4]Christophe Merieux Laboratory, Institute of Pathogen Biology, Chinese Academy of Medical Sciences and Peking Union Medical College, 100730 Beijing, P.R. China.

[5]Center for Regenerative Medicine, Massachusetts General Hospital, Boston, MA, USA. Harvard Stem Cell Institute, Harvard University, Cambridge, MA, USA. Department of Medicine, Massachusetts General Hospital, Harvard Medical School, Boston, Massachusetts, USA.

[6]CAS Key Laboratory of Pathogenic Microbiology and Immunology, Institute of Microbiology, Chinese Academy of Sciences, Beijing 100101, China

[7] Key Laboratory of Cell Proliferation and Differentiation of the Ministry of Education, School of Life Sciences, Peking University, Beijing 100871, China; Peking-Tsinghua Center for Life Sciences, Peking University, Beijing 100871, China.

[8]e-mail: zhouzhuo@pku.edu.cn, wswei@pku.edu.cn, wangjw28@163.com

*These authors contributed equally to this work.

Abstract

The global coronavirus disease 2019 (COVID-19) pandemic is caused by severe acute respiratory syndrome coronavirus 2 (SARS-CoV-2), a positive-sense RNA virus. How the host immune system senses and responds to SARS-CoV-2 infection remain to be determined. Here, we report that SARS-CoV-2 infection activates the innate immune response through the cytosolic DNA sensing cGAS-STING pathway. SARS-CoV-2 infection induces the cellular level of 2'3'-cGAMP associated with STING activation. cGAS recognizes chromatin DNA shuttled from the nucleus as a result of cell-to-cell fusion upon SARS-CoV-2 infection. We further demonstrate that the expression of spike protein from SARS-CoV-2 and ACE2 from host cells is sufficient to trigger cytoplasmic chromatin upon cell fusion. Furthermore, cytoplasmic chromatin-cGAS-STING pathway, but not MAVS-mediated viral RNA sensing pathway, contributes to interferon and pro-inflammatory gene expression upon cell fusion. Finally, we show that cGAS is required for host antiviral responses against SARS-CoV-2, and a STING-activating compound potently inhibits viral replication. Together, our study reported a previously unappreciated mechanism by which the host innate immune system responds to SARS-CoV-2 infection, mediated by cytoplasmic chromatin from the infected cells. Targeting the cytoplasmic chromatin-cGAS-STING pathway may offer novel therapeutic opportunities in treating COVID-19. In addition, these findings extend our knowledge in host defense against viral infection by showing that host cells' self-nucleic acids can be employed as a "danger signal" to alarm the immune system.

Introduction

The outbreak of COVID-19 caused by SARS-CoV-2[1,2] poses a great threat to global public health. To date, the knowledge on the molecular pathogenesis of SARS-CoV-2 is limited, thwarting the development of therapeutic and prevention strategies. Since innate immunity plays pivotal roles in both host defense and viral immunopathology, understanding the roles of innate immunity involved in SARS-CoV-2 infection is an important biomedical objective.

Activation of the innate immune system upon viral infection is generally thought to be initiated by recognizing specific viral components, termed as pathogen-associated molecular patterns (PAMPs) that are recognized by host pattern recognition receptors (PRRs)[3]. Viral genetic materials, such as genomic RNA, are detected by RIG-I-like receptors (RLRs), including RIG-I or MDA5, and the Toll-like receptors (TLRs). In contrast, viral genomic DNA exposed in the cytosol is detected by cGAS. Upon activation, RLRs and cGAS recruit adaptor molecules MAVS and STING, respectively, to activate downstream signaling pathways that eventually trigger the expression of antiviral or immunoregulatory cytokines, such as interferons (IFNs)[4]. In addition to sensing viral components, the RLRs and cGAS pathways are reported to mediate sterile inflammation in the absence of infection induced by self-nucleic acids, such as in autoimmune disorders[5]. Whether host nucleic acids can mediate antiviral immunity is poorly understood.

SARS-CoV-2, an RNA virus, has evolved multi-level strategies to evade the RLR-sensing/signaling pathway to permit its replication in host cells. Multiple proteins encoded by SARS-CoV-2, including ORF3, ORF6, M, and several non-structure proteins, inhibit RLR-induced IFN activation[6-8]. Moreover, SARS-CoV-2 papain-like protease and M protein were shown to suppress MDA5 and MAVS activity, respectively[9,10]. These viral antagonistic mechanisms may account for the dampened type-I IFN (IFN-I) levels in some severe COVID-19 cases[11]. Despite these inhibitory machineries exploited by the virus, overt IFN activation and inflammatory responses were still detected in SARS-CoV-2-infected animals[12,13] and peripheral blood or respiratory tract samples from COVID-19 patients[14-18]. A major gap in our knowledge is how SARS-CoV-2 infection triggers host innate immune responses.

Here we report that the cytosolic DNA sensing cGAS-STING pathway is involved in IFNs production upon SARS-CoV-2 infection. The activation of cGAS relies on its recognition of cytoplasmic chromatin DNA generated upon cell-to-cell fusion, a widespread phenomenon in

SARS-CoV-2-infected cells[19], organoids[20], animals[21], and in COVID-19 patients[22]. Our study revealed a mechanism, distinct from the classical PAMP-PRR paradigm, by which the host innate immune system responds to viral infection by producing "danger signals" using self-materials.

SARS-CoV-2 infection activates the cGAS-STING pathway

We recently reported that SARS-CoV-2 infection failed to induce rapid IFN-β production in cultured cells[6], consistent with multiple inhibitory mechanisms against the RLR pathway imposed by the virus. Mysteriously, however, SARS-CoV-2 induces substantial IFN-β production at later time points of infection[6]. These observations prompted us to hypothesize that a signaling pathway distinct from the RLR signaling is activated. Among the major host innate immune mechanisms that stimulate IFNs production is the cGAS-STING cytosolic DNA sensing pathway. Thus, we asked whether SARS-CoV-2 infection activates cGAS and STING. We infected human lung epithelial cell line Calu-3 and HeLa cells expressing ACE2 (HeLa-ACE2) with SARS-CoV-2, and then examined the phosphorylation of STING at Ser366 (phospho-STING^{Ser366}), a hallmark of STING activation[23]. At 8 h post-infection, phospho-STING^{Ser366} was barely detected in Calu-3 and HeLa-ACE2 cells, while after infection for 16 h, both cell lines showed robust STING^{Ser366} phosphorylation (Fig. 1a, b). In line with this, cyclic dinucleotide 2'3'-cGAMP, a molecule produced by activated cGAS, was significantly increased after 16 h of infection (Fig. 1c). Hence, the cGAS-cGAMP-STING cascade is activated during SARS-CoV-2 infection.

As a comparison, we examined whether other RNA viruses can activate STING. In contrast to SARS-CoV-2, Sendai virus (SeV), a well-characterized agonist of the RLR signaling pathway, failed to stimulate STING ^{Ser366} phosphorylation despite its competent viral replication (Fig. 1d, e). Of note, at 8 h post-infection, SeV substantially stimulated phosphorylation of IRF3 (Fig. 1d, e), a downstream protein for both RLR-MAVS and cGAS-STING pathways. In contrast, IRF3 phosphorylation was weakly stimulated after SARS-CoV-2 infection at 8 h, while it was sharply increased after infection at 16 h (Fig. 1a, b, and e); the kinetic of IRF3 phosphorylation is consistent with that of STING phosphorylation. These observations suggest that SARS-CoV-2 counteracts RLR detection/signaling upon early phase of infection, but effectively stimulates the cGAS-STING pathway upon late phase of infection.

We subsequently asked whether STING-mediated signaling is required for SARS-CoV-2-

triggered interferon responses. While SARS-CoV-2 infection into Calu-3 cells induced the expression of IFN and IFN-stimulated genes (ISGs), including *IFNB*, *IFIT1*, *ISG15*, and *CCL5,* pharmacological inhibition of STING by an established compound, H-151[24], significantly decreased SARS-CoV-2-triggered interferon responses (Fig. 1f). Hence, STING is not only activated but is also required for interferon production upon SARS-CoV-2 infection.

cGAS colocalizes with cytosolic genomic DNA in SARS-CoV-2-induced syncytia

We next sought to determine how SARS-CoV-2 infection activates the cGAS-STING pathway. The genetic entity of SARS-CoV-2 is RNA, which does not stimulate cGAS. Recent studies suggested that cGAS can detect self-DNA presented in the cytosol, including chromosomal DNA[25-28] and mitochondrial DNA[29]. We thus hypothesized that cGAS is activated by self-DNA upon SARS-CoV-2 infection. Using fluorescent microscopy, we found that a prominent cellular morphology feature in response to SARS-CoV-2 infection is cell-cell fusion and the formation of syncytia (a single cell containing several nuclei) (Extended Data Fig. 1a). SARS-CoV-2 enters host cells by membrane fusion dependent on the interaction between viral spike protein and cell surface protein ACE2[30]. During subsequent viral replication, the infected cells can form syncytia mediated by cell surface expression of spike protein[19]. We found that, at 20 h post-infection, nearly 20% of total HeLa-ACE2 cells were fused to form multinucleated cells (Extended Data Fig. 1b). SARS-CoV-2-induced cell fusion was further observed in other cell types, including lung epithelial cell Calu-3 and THP-1 macrophages (Extended Data Fig. 1c). Immuno-staining of SARS-CoV-2-infected cells with antibodies against viral nucleocapsid protein (NP) and Lamin B1 that marks the nuclear envelope revealed that cell fusion led to close contact among nuclei (Extended Data Fig. 1d). Upon staining of DNA with DAPI, we observed nuclear membrane blebbing (Fig. 2a, upper) accompanied by budding off nuclei (Fig. 2a, lower) in the fused cells. We quantified the frequency of cytoplasmic DAPI events in fused cells and non-fused cells and found that cytoplasmic DAPI events are predominantly observed in fused cells (Fig. 2b), indicating that cell fusion promotes the generation of cytoplasmic genomic DNA.

The nuclear membrane blebbing and nucleus-to-cytoplasm trafficking of genomic DNA observed upon SARS-CoV-2 infection are reminiscent of cytoplasmic chromatin in cellular senescence. In senescent cells, fragments of chromatin are shuttled to the cytoplasm, via nuclear

membrane blebbing[31], and are recognized by cGAS[27,28,32]. We and others reported that cytoplasmic chromatin activates the cGAS-STING pathway, stimulating the pro-inflammatory responses of senescence[27,28,32]. In addition to senescence, cytoplasmic chromatin is observed in cancer, aging, and other stressed conditions, leading to cGAS activation[33,34]. We therefore hypothesized that cytoplasmic chromatin upon SARS-CoV-2 infection activates cGAS.

We subsequently examined the localization of cGAS. In non-infected cells, cGAS showed a diffuse distribution in both cytoplasm and nucleus (Fig. 2c and Extended Data Fig. 1e). Upon SARS-CoV-2 infection, in fused cells staining positive for NP, cGAS displayed nuclear distribution and aggregated to form puncta that colocalize with cytoplasmic chromatin (Fig. 2c and Extended Data Fig. 1e); cGAS did not form cytoplasmic aggregation in non-fused cells (Fig. 2c and Extended Data Fig. 1e). The colocalization between cytoplasmic chromatin and cGAS is consistent with the generation of cGAMP in infected cells (Fig. 1c). Moreover, STING redistributed from endoplasmic reticulum to confined compartments in fused cells, typical for STING activation (Fig. 2d). Taken together, these results indicate that cytoplasmic genomic DNA formed in syncytia activates the cGAS-STING pathway upon SARS-CoV-2 infection.

Cell fusion in the absence of viral infection activates the cGAS-STING pathway

We next asked whether cell fusion *per se* can provoke antiviral responses in the absence of viral infection. To address this, we developed a co-culture system to recapitulate SARS-CoV-2-induced cell fusion. HEK293T cells were transfected with plasmids expressing EGFP and spike protein of SARS-CoV-2 and were mixed with HeLa-ACE2 cells expressing mCherry (illustrated in Fig. 3a). As measured by the amounts of EGFP/mCherry double-positive cells, we found that spike protein stimulates cell fusion in a dose-dependent manner (Fig. 3b). We then examined the expression of genes involved in antiviral responses. Cell fusion *per se* mediated by Spike and ACE2 potently induced the expression of cytokines/ISGs, including *IFNB*, *ISG15*, *IL8*, and *CCL5* (Fig. 3c). The induction of antiviral genes is dependent on cell fusion rather than spike expression, because co-culture of HEK293T cells expressing spike protein (HEK293T(S)) with wild-type HeLa cells that do not express ACE2 (Extended Data Fig. 2a) failed to trigger cell fusion (Extended Data Fig. 2b) and cytokines/ISGs expression (Extended Data Fig. 2c). Thus, cell fusion mediated by Spike and ACE2 activates innate immune response in the absence of viral infection.

We subsequently examined the status of cGAS and STING in the co-culture system. We found that the co-culture of HEK293T(S) cells with HeLa-ACE2 cells, rather than wild-type HeLa cells, activated STING, as detected by the formation of STING homodimers, the active form of STING (Fig. 3d and Extended Data Fig. 2d). Concomitantly, cell fusion resulted in IRF3 phosphorylation (Fig. 3d and Extended Data Fig. 2d), suggesting the activation of the STING-IRF3 signaling axis. We further examined whether cGAS and STING are required for cell fusion-triggered antiviral signaling. In the co-culture system, genetic ablation of cGAS in HeLa-ACE2 cells (HeLa-cGAS^{KO}-ACE2, Extended Data Fig. 2e) suppressed *IFNB* induction (Fig. 3e) and IRF3 phosphorylation (Fig. 3f) without affecting cell fusion (Extended Data Fig. 2f). Re-expression of cGAS in cGAS-null cells (HeLa-cGAS^{RE}-ACE2, Extended Data Fig. 2e) rescued *IFNB* expression (Fig. 3e) and IRF3 phosphorylation (Fig. 3f). Genetic depletion of STING (Extended Data Fig. 2g) phenocopied the effect of cGAS (Fig. 3e, f). In contrast, MAVS, the adaptor protein critical for RLR-mediated signaling, is dispensable for cell fusion-induced IFN activation (Extended Data Fig. 3h and Fig. 3e, f). Therefore, we conclude that the cGAS-STING pathway is required for cell fusion-induced IFN and pro-inflammatory responses.

Sensing of cytoplasmic chromatin by cGAS in syncytial cells

We examined the mechanisms for cGAS activation in syncytial cells in the absence of infection, and hypothesized that cytoplasmic chromatin activates cGAS. We co-cultured HeLa-ACE2 cells expressing cGAS-HA with HEK293T(S) cells, followed by cGAS-HA and DNA co-staining. Using confocal fluorescent microscopy, we found that multiple DNA-containing puncta appeared in the perinuclear region and are partially colocalized with cGAS in the fused cells (Fig. 4a). In some cases, cGAS colocalized with nuclear DNA that is in the process of budding off the nucleus (Fig. 4a, Inset 2). To dissect this process in more depth, we generated three-dimensional reconstructed images, co-staining for Lamin B1, cGAS, and DNA. This analysis showed that a hemispheric body containing cGAS and chromosomal DNA is localized at the fringe of the nucleus and is beneath or in the process of penetrating the nuclear lamina meshwork, representing a typical nuclear membrane bleb (Fig. 4b). We further performed live-cell imaging to document this dynamic process. HeLa-ACE cells expressing cGAS-GFP were co-cultured with HEK293T cells expressing cGAS-GFP and spike, and were stained with DRAQ5 for live-cell imaging of DNA. This experiment revealed that cell

fusion leads to the formation of nuclear membrane blebs accompanied by subsequent budding off to form cytoplasmic chromatin (Fig. 4c, d). In some cases, cGAS was recruited to cytoplasmic chromatin after nuclear membrane blebs budded off nuclei (Fig. 4c and Extended data Movie 1). In other cases, cGAS was recruited to intra-nuclear chromatin that is in the process of nucleus-to-cytoplasm trafficking and was co-shuttled to the cytoplasm (Fig. 4d and Extended data Movie 2).

Because cytoplasmic chromatin in the context of senescence is associated with DNA damage response[28], we next examined if cell fusion-induced cytoplasmic chromatin stains positive for DNA damage markers. By staining co-cultured cells for DNA damage marker γH2AX, we found that cGAS strongly co-colocalizes with γH2AX puncta in the cytoplasm and occasionally in the nucleus (Fig. 4e and Extended data Fig. 3). Three-dimensional reconstructed images, focusing on nuclear events, showed that γH2AX colocalizes with cGAS at the budding chromatin undergoing nucleus-to-cytoplasm transport (Extended data Fig. 3). In sum, we reported that cytoplasmic chromatin is sensed by cGAS in syncytia mediated by spike and ACE2.

Targeting cGAS-STING pathway as potential therapeutics against SARS-CoV-2

Lastly, we investigated the role of the cGAS-STING pathway in restraining SARS-CoV-2 replication in host cells. HeLa-ACE2, HeLa-cGAS^{KO}-ACE2, and HeLa-cGAS^{RE}-ACE2 cells were infected with SARS-CoV-2. At 12 h post-infection, depletion of cGAS did not affect virus replication, while re-expression of cGAS in cGAS-null cells showed antiviral effects (Fig. 5a), possibly due to overexpression of cGAS (Fig. 5a). At 24 h post-infection, cGAS depletion led to significantly elevated viral replication (Fig. 5a), indicating that cGAS-mediated signaling is required for optimal host defense against SARS-CoV-2. The antiviral role for cGAS at a later time point coincides with the timeframe required for cell-to-cell fusion, which occurs around 12-14 hours post-infection.

Recently, STING agonists were pre-clinically or clinically tested as antitumor drugs due to their immunostimulatory effects[35]. We therefore examined whether STING agonists can be harnessed as antiviral drugs against SARS-CoV-2. diABZI, a recently developed synthetic non-nucleotide STING agonist[36] (Fig. 5b), exerts potent antiviral activity against SARS-CoV-2 with half-maximal inhibitory concentration (IC_{50}) values of 0.023 μM in Calu-3 cells (Fig. 5c) and 0.061 μM in HeLa-ACE2 cells (Fig. 5d). This diABZI-mediated antiviral efficacy is comparable to that

of Remdesivir (IC50 = 0.054 in Calu-3 and 0.024 μM in HeLa-ACE2) (Extended data Fig. 4), a direct-acting antiviral drug against SARS-CoV-2. Taken together, these results strongly suggest an antiviral role for the cGAS-STING pathway in restraining SARS-CoV-2.

Discussion

Our study revealed that host self-DNA, distinct from pathogen genetic molecules, can serve as a danger signal to trigger antiviral responses in SARS-CoV-2 infection. This response relies on SARS-CoV-2-induced syncytia, which causes nuclear export of chromosomal DNA that activates the cytosolic DNA sensing cGAS-STING pathway. This finding expands the horizon of how innate immune system reacts to pathogen infection, beyond the established PAMP-PRR model. Because viruses possess multiple mechanisms to inhibit PAMP-PRR sensing/signaling, the host cells have evolved a mechanism that produces danger signals using self-constituents. This mechanism offers additional routes to permit communication with neighboring cells and the immune system upon viral infection. This new perspective of innate immune defense in mammalian systems may be exploited to restrain other viruses.

Cell fusion can be observed during infection by a panel of enveloped viruses[37,38]. Besides viral infection, cell fusion is involved in other biological processes such as embryogenesis, tissue morphogenesis[39], and cancer[40]. In addition, ectopic expression of proteins that drive cell fusion promotes senescence of primary cells associated with pro-inflammatory responses[41]. A commonality of these pathophysiological conditions is the secretion of growth factors/cytokines. It is thus valuable to investigate whether formation of cytoplasmic chromatin is involved in these cell fusion events.

Chromosomal DNA in the cytoplasm can be generated by chromosome mis-segregation during cell division, such as micronuclei[25,26], or by nucleus-to-cytoplasm transport of chromatin fragments under certain pathological conditions such as cellular senescence[27,28]. In SARS-CoV-2-induced syncytia, no cell division was observed under live-cell imaging experiments (Fig. 2c and Extended Fig. 1e), and hence the cytoplasmic chromosomal DNA does not fit into the criteria of micronuclei. Instead, the nuclear membrane blebbing and subsequent partition into the cytoplasm in SARS-CoV-

2 infected cells are akin to the generation of cytoplasmic chromatin fragments (CCFs) in senescence[31]. CCFs in senescence stain positive for repressive heterochromatin marks and negative for active euchromatin marks and are positive for γH2AX[31], indicating that CCFs are derived from fragments of chromatin and are associated with DNA damage response. While senescence is usually established in primary cells in days to weeks, cytoplasmic chromatin observed during SARS-CoV-2 infection occurs within hours and can be seen in transformed cancer cells, suggesting that the infected cells may not require senescence to induce pro-inflammatory responses. However, senescence and SARS-CoV-2-induced syncytia do share similar molecular features, such as the DNA damage response and possibly other cell stress pathways, indicating that common mechanisms may be involved to generate cytoplasmic chromatin in both scenarios. The molecular mechanisms for generating cytoplasmic chromatin in senescence and SARS-CoV-2 infection are poorly understood and represent a future direction for research.

Because coronaviruses are sensed by RLRs or TLRs[42], it remains to be determined whether SARS-CoV-2 can be recognized by those RNA sensors. As SARS-CoV-2 robustly inhibits RLR-mediated IFN activation[6], the host could leverage syncytia-associated cytoplasmic chromatin-cGAS-STING pathway to stimulate IFN responses to curb SARS-CoV-2 replication. Indeed, we showed that cGAS potentiates host defense against SARS-CoV-2. Moreover, diABZI, a STING agonist, exerts potent antiviral effects against SARS-CoV-2. Considering that SARS-CoV-2 possesses countermeasures to block IFN activity[6], and that STING can restrict virus replication by IFN-independent mechanisms such as translation inhibition[43] and autophagy[44], we reason that STING agonist-based therapies may offer new opportunities to treat COVID-19.

On the other hand, cytoplasmic chromatin can trigger inflammation that contributes to tissue damage and disease progression[28,45]. In addition, syncytial cells can undergo cell death that may further incite inflammation. Importantly, large multinucleated pneumocytes are frequently found in post-mortem samples from COVID-19 patients[22,46]. Therefore, syncytia formation may contribute to immunopathological outcomes such as hypercytokinemia in COVID-19 patients. In this scenario, inhibitors targeting cGAS-STING or cell fusion may suppress inflammation-associated disorders in COVID-19 patients. Future studies are needed to unravel the disease stages of COVID-19 that are

likely to be responsive to targeting the pathway we discovered herein.

Figure legends

Fig. 1: SARS-CoV-2 infection activates the cGAS-STING pathway

a, b Representative Western blots of STING and IRF3 phosphorylation upon SARS-CoV-2 infection (n = 2 independent experiments). Calu-3 (**a**) or HeLa-ACE2 (**b**) cells were mock-infected or infected with SARS-CoV-2 at an MOI of 0.5. At indicated time points after infection, cells were harvested and lysed. Lysates were then subjected to Western blot analysis using indicated antibodies. ★ Activated STING. **c** 2'3'-cGAMP levels in cells infected with SARS-CoV-2. HeLa-ACE2 were infected with SARS-CoV-2 as described in (**b**). A competitive ELISA assay determined the 2'3'-cGAMP concentrations. Mean ± s.d., n = 3 independent experiments. $^{**}P < 0.01$, n.s., not significant. Two-tailed Student's *t*-test on log-transformed data. **d** STING and IRF3 phosphorylation upon SeV infection. HeLa-ACE2 cells were mock-infected or infected with SeV. Cells were harvested at indicated times and analyzed by Western blot. **e** Semi-quantitative analysis on Western blot results from (**a**) and (**d**) by densitometry. **f** Calu-3 cells were treated with DMSO or 200 ng/ml of H-151. After 2 h, cells were mock-infected or infected with SARS-CoV-2 at an MOI of 0.5 for 24 h. RNA extracted from the cells was evaluated by quantitative PCR. The data are expressed as fold change of the *IFNB*, *IFIT1*, *ISG15*, and *CCL5* mRNA levels relative to the *GAPDH* control. Mean ± s.d., n = 3 independent experiments. $^{*}P < 0.05$, $^{**}P < 0.01$, two-tailed Student's *t*-test.

Fig. 2: cGAS colocalizes with cytosolic genomic DNA in SARS-CoV-2-induced syncytia

a Representative confocal immunofluorescence images of SARS-CoV-2-induced syncytia. HeLa-ACE2 cells stably expressing mCherry were infected with SARS-CoV-2 at an MOI of 0.5. After 18 h, cells were fixed and stained for DNA with DAPI (blue) and viral nucleocapsid protein (NP) with anti-NP antibody (green). Triangles indicate budding chromatin (upper) or cytosolic chromatin (lower). **b** Quantification of cells for parameters as indicated. Cells were quantified for three different fields with 200 cells. Mean ± s.d., n = 3 independent experiments. $^{**}P < 0.01$, two-tailed Student's *t*-test. **c** Representative images of cells stained for NP, DNA, and cGAS-Flag. cGAS-null HeLa-ACE2 cells reconstituted with cGAS-Flag were infected with SARS-CoV-2 at an MOI of 0.5 for 18 h, followed by staining with anti-NP antibody (green), DAPI (blue), and anti-cGAS antibody

(red) as indicated. **d** Representative images of cells stained for ER and STING. HeLa-ACE2 cells were treated as described in (**c**) and were stained with anti-calcineurin (red) antibody and anti-STING (green) antibody as indicated. Scale bar, 20 μm

Fig. 3: Cell fusion activates the innate immune response via the cGAS-STING pathway

a Scheme of co-culture experiment. **b** Representative fluorescence images of co-culture experiment. HEK293T cells were transfected with vector control (Vec) or increasing amounts of plasmids expressing EGFP and spike for 24 h. Cells were then detached and mixed with HeLa-ACE2 expressing mCherry (HeLa-ACE2-mCherry). After 8 h, cells were subjected to fluorescence microscopy analysis. Scale bar, 250 μm. **c** Cytokine genes/ISGs expression in co-cultured cells. Cells were co-cultured as indicated in (**b**). RNA extracted from the cells was evaluated by quantitative PCR. The data are expressed as fold change of the *IFNB*, *ISG15*, *IL8* and *CCL5* mRNA levels relative to the *GAPDH* control. Mean ± s.d., n = 4 independent experiments. $^{**}P < 0.01$, $^{***}P < 0.001$, $^{****}P < 0.0001$, two-tailed Student's *t*-test. **d** Western blot analysis of cells from co-culture experiment as described in (**b**) using indicated antibodies. STING blots were performed under non-reducing (top) or reducing conditions. ★ STING dimer. **e** HEK293T cells were transfected with vector control (Vec) or plasmids expressing spike. After 24 h, cells were detached and mixed with HeLa-ACE2-mCherry cells as indicated. $cGAS^{KO}$, $STING^{KO}$, and $MAVS^{KO}$ represent cells depleted of indicated genes. $cGAS^{RE}$ represents cGAS-null cells re-expressed cGAS. The expression of *IFNB* mRNA was assayed as described in (**c**). Mean ± s.d., n = 3 independent experiments. $^{**}P < 0.01$, $^{****}P < 0.0001$, n.s., not significant. two-tailed Student's *t*-test. **f** Western blot analysis of cells from the co-culture experiment as described in (**e**). ★ ACE2 fragments generated during cell co-culture. S, Spike.

Fig. 4: cGAS is colocalized with cytoplasmic chromatin in syncytial cells

a Representative confocal immunofluorescence images of co-cultured cells stained for DNA and cGAS-HA. HEK293T cells transfected with plasmids expressing S (HEK293T(S)) were co-cultured with cGAS-null HeLa-ACE2 cells reconstituted with cGAS-HA. After 8 h, cells were stained with DAPI (blue) and anti-HA (red) antibody as indicated. Triangles indicate colocalization of cGAS with cytosolic chromatin. **b** Representative confocal immunofluorescence images of co-cultured

cells stained for DNA, cGAS-HA, and Lamin B1. Co-culture experiments were performed as described in (**a**). Cells were stained with DAPI (blue), anti-HA (red), and anti-Lamin B1 (green) antibodies. Three-dimensional reconstructed images based on z-stack images were displayed as volume view. **c**, **d** Extracted frames from live-cell imaging of co-cultured cells using confocal microscopy. HEK293T(S) cells transfected with plasmids expressing cGAS-GFP were co-cultured with cGAS-null HeLa-ACE2 cells transfected with plasmids expressing cGAS-GFP. After 1 h, cells were stained with DRAQ5 (purple) for visualizing DNA and subjected to live-cell imaging. **e** Co-culture experiments were performed as described in (**a**). Cells were stained with DAPI (blue), anti-HA (red) antibody, and anti-γ-H2AX (green) antibody. Scale bar, 20 μm or (inset) 5 μm.

Fig.5: Targeting cGAS-STING pathway as potential therapeutics against SARS-CoV-2

a Effect of cGAS expression on SARS-CoV-2 replication. Wild-type HeLa-ACE2 (WT), HeLa-cGAS^{KO}-ACE2, and HeLa-cGAS^{RE}-ACE2 cells were infected with SARS-CoV-2 at an MOI of 0.5. At indicated times, total RNA extracted from cells was evaluated by quantitative PCR. The data are expressed as fold changes of the RNA levels of the viral *N* gene relative to the *GAPDH* control. Mean ± s.d., n = 3. **P* < 0.05, ***P* < 0.01, *****P* < 0.0001, n.s., not significant. two-tailed Student's *t*-test. **b** The chemical structure of diABZI. **c**, **d** Antiviral effect of diABZI on SARS-CoV-2. Calu-3 (**c**) or HeLa-ACE2 (**d**) Cells were treated with serially diluted diABZI for 24 h (Calu-3) or 1 h (HeLa-ACE2). Cells were then subjected to viability assay or infected with SARS-CoV-2 at an MOI of 0.2. After 24 h (Calu-3) or 48 h (HeLa-ACE2). Supernatants were harvested for RNA extraction, followed by absolute quantification of viral *N* mRNA by PCR. Mean ± s.d., n = 4. The IC_{50} (The half-maximal inhibitory concentration) and CC_{50} (The half-maximal cytotoxic concentration) values were calculated using Prism software.

Methods

Viruses and Cells.

HEK293T (ATCC, #CCL-11268), HeLa (ATCC, #CCL-2), Calu-3 (ATCC, #HTB-55), HeLa-ACE2, HeLa-cGAS^{KO}-ACE2, HeLa-cGAS^{RE}-ACE2, HeLa-STING^{KO}-ACE2, and HeLa-MAVS^{KO}-ACE2 cells were maintained in Dulbecco's modified Eagle's medium (Gibco) supplemented with 10% (vol/vol) FBS (Biological Industries) and antibiotics. The THP-1 cells (ATCC #TIB-202) were

maintained in RPMI1640 (HyClone) supplemented with 10% (vol/vol) FBS (Gibco) and antibiotics. HeLa-cGAS^{KO}-ACE2 cells and HeLa-cGAS^{RE}-ACE2 cells were generated by lentiviral transduction of HeLa-cGAS^{KO} and HeLa-cGAS^{RE} cells[47] with ACE2. HeLa-STING^{KO}-ACE2 cells and HeLa-MAVS^{KO}-ACE2 cells were generated by lentiviral transduction of CRISPR-Cas9-engineered HeLa-STING^{KO} and HeLa-MAVS^{KO} cells with ACE2. SARS-CoV-2 virus infection was performed as described previously[6]. All experiments with the SARS-CoV-2 virus were conducted in the BSL-3 laboratory.

Lentivirus Packaging and Infection

The plasmid expressing ACE2 and mCherry, together with lentiviral packaging plasmids pVSVG and pR8.74 (Addgene), was transfected into HEK293T cells using the X-tremeGENE HP DNA transfection reagent (Roche, 06366546001) to produce the lentivirus. HeLa cells were infected with lentivirus at an MOI > 1 for 72 h and were then subjected to FACS sorting to enrich mCherry positive cells.

Co-culture Experiment

HEK293T cells were plated 24 h before transfection at a density of 1.5×10^5 cells per well in the 24-well plate and were transfected with SARS-CoV-2 Spike expression plasmid. HeLa-ACE2 cells were seeded at a density of 100,000 cells per well in the 24-well plate. Twenty-four h after transfection, 5×10^5 HEK293T cells were seeded onto HeLa-ACE2 cells and co-cultured for the indicated period.

Plasmids and Reagents

SARS-CoV-2 spike (S) expression plasmid was described previously[6]. The HA-tagged and GFP-tagged cGAS constructs were described previously[48]. DRAQ5 (ab108410) was purchased from Abcam. DAPI (4',6-diamidino-2-phenylindole) (40728ES03) was from YEASEN. STING-specific inhibitor H-151 (inh-h151) was from InvivoGen. diABZI STING agonist (compound 3) (S8796) was from Selleck.

Immunoblotting

Cells were lysed, and an equal amount of each lysate was subsequently analyzed by SDS–PAGE following standard procedures. The antibodies used for immunoblotting were: rabbit anti-cGAS (D1D3G, #15102S, Cell Signaling Technology, 1:500), rabbit anti-STING (D2P2F, #13647S, Cell Signaling Technology, 1:500), rabbit anti-phospho-STING (Ser366) (D7C3S, #19781S, Cell Signaling Technology, 1:500), rabbit anti-IRF3 (ab76409, Abcam, 1:1000), rabbit anti-phospho-IRF3 (ab76493, Abcam, 1:1000), rabbit-anti-GAPDH (BE0024, EASYBIO, 1:2000), mouse-anti-β-Tubulin (CW0098, CWBIO, 1:2000), rabbit-anti-SARS-CoV-2 spike protein (40589-T62, Sino Biological, 1:1000), rabbit-anti-SARS-CoV-2 nucleocapsid protein (NP) (40143-R019, Sino Biological, 1:1000), rabbit-anti-Sendai virus (PD029C1, MBL, 1:1000), rabbit-anti-ACE2 (10108-T60, Sino Biological, 1:1000), mouse-anti-MAVS (sc166583, Santa Cruz, 1:500), goat-anti-mouse IgG-HRP secondary antibody (115035003, Jackson ImmunoResearch), goat-anti-rabbit IgG-HRP secondary antibody (111035003, Jackson ImmunoResearch). For STING dimer detection, reducing reagents were not added to the lysates, and samples were not heated before loading.

Real-time PCR

Total RNA was extracted using RNAprep Pure Micro Kit (DP420, TIANGEN) and reverse-transcribed using the Quantscript RT Kit (KR103, TIANGEN). Real-time quantitative PCR was performed using SYBR green kit (Takara Bio, RR820A). The following primers were used for real-time PCR: *GAPDH*-F: 5'-GGCATGGACTGTGGTCATGAG-3', *GAPDH*-R: 5'-TGCACCACCAACTGCTTAGC-3', *IFNB*-F: 5'-ACGCCGCATTGACCATCTAT-3', *IFNB*-R: 5'-TAGCCAGGAGGTTCTCAACA-3', *IL8*-F: 5'-CCACCGGAAGGAACCATCT-3', *IL8*-R: 5'-GGCCAGCTTGGAAGTCATGT-3', *ISG15*-F: 5'- GAGAGGCAGCGAACTCATCT-3, *ISG15*-R: 5'-CTTCAGCTCTGACACCGACA-3', *CCL5*-F:5'- CCCAGCAGTCGTCTTTGTCA-3', *CCL5*-R: 5'- TCCCGAACCCATTTCTTCTCT-3'. *IFIT1*-F: 5'-TACAGCAACCATGAGTACAA-3', *IFIT1*-R: TCAGGTGTTTCACATAGGC,

Absolute quantitative PCR for viral *N* mRNA

Calu-3 or HeLa-ACE2 cells were treated with indicated drugs, followed by SARS-CoV-2 infection. At 24 h (Calu-3) or 48 h (HeLa-ACE2) post-infection, supernatants were collected and subjected to RNA extraction using Direct-zol RNA MiniPrep kit (Zymo research, CA, USA) according to the

manufacturer's instructions. Viral copy numbers were measured by RT-PCR using primers and probes targeting the SARS-CoV-2 *N* gene. The reference standard was serially diluted by tenfold from 1×10^9 copies to 1×10^4 copies. PCR amplification procedure was 50°C, 15min, 95°C, 3min; 95°C, 15s, 60°C, 45s, 50 cycles, and data were processed by Bio-Rad CFX Manager software. The Primer sequence specific for SARS-CoV-2 *N* was available from J.W. upon request.

IC_{50} and CC_{50} determination

Calu-3 or HeLa-ACE2 cells were seeded in 96-well plates one day before infection. For IC_{50} determination, cells were pre-treated with drugs at concentrations of 0.013, 0.041, 0.123, 0.370, 1.111, 3.333, 10, and 30 μM for 24 h (Calu-3) or 1 h (HeLa-ACE2). Cells were then subjected to viability assay or infected with SARS-CoV-2 at an MOI of 0.2. After 24 h (Calu-3) or 48 h (HeLa-ACE2), supernatants were harvested for RNA extraction, followed by absolute quantification of viral *N* mRNA by quantitative PCR. The inhibition ratio was obtained by dividing the viral copy number in drug-treated samples by those in the vehicle control samples. For CC_{50} determination, cells were pre-treated with each drug at indicated concentrations and time points. Cell viability was evaluated using a CCK8 kit (Yeasen, Beijing, China) according to the manufacturer's instructions. The IC_{50} and CC_{50} values were calculated using Prism (Graphpad Software Inc.).

Immunofluorescence

Cells were washed with PBS buffer and fixed with 4% paraformaldehyde (PFA) in PBS for 20 min at room temperature. Cells then were permeabilized with 0.5% Triton X-100 and blocked in blocking buffer comprising 5% bovine serum albumin (BSA). Cells were stained with primary antibodies, followed by staining with second antibodies, including Alexa Fluor 488 AffiniPure Goat Anti-Rabbit IgG (H+L) (111545003, Jackson ImmunoResearch), Goat anti-Mouse IgG (H+L) Highly Cross-Adsorbed Secondary Antibody (A16080, Thermo Fisher), and Alexa Fluor Plus 647 (A32728, Thermo Fisher). The primary antibodies used in this research were: mouse anti-SARS-CoV-2 Nucleoprotein (40143-MM08, Sino Biological), rabbit anti-STING (D2P2F, #13647S, Cell Signaling Technology), mouse-anti-Calcineurin (C0581, Sigma-Aldrich), rabbit-anti-γ-H2AX (20E3, #9718S, Cell Signaling Technology), rabbit-anti-Lamin B1 (ab16048, Abcam), mouse-anti-HA (CW0092, CWBIO). Fluorescence images were obtained and analyzed using Leica

Microsystems (LAS X) or Dragonfly Spin-disk system (ANDOR) on a Leica DMi8 microscope. Three-dimensional images were obtained from z-stack images collected at 0.2 μm intervals and processed by ImageJ. For live-cell imaging, HeLa-ACE2 cells were transfected with cGAS-GFP and were then co-cultured with HEK293T cells transfected with cGAS-GFP and spike. After 1 h, cells were stained with DRAQ5 (1:250) and subjected to live-cell imaging. Images were recorded every 1 min for 3.5 h and analyzed by the Fusion 2.0 software (ANDOR) and ImageJ.

Quantification of 2'3'-cGAMP

SARS-CoV-2-infected cells were lysed in mPER lysis buffer (78501, Thermo Fisher) and heated to inactivate the virus. For 2′3′-cGAMP measurement, an ELISA kit based on the competition between 2′3′-cGAMP and a 2′3′-cGAMP-horseradish peroxidase conjugate (501700, Cayman Chemical) was used according to the manufacturer instructions.

Statistics

Statistical analysis was performed using Prism (Graphpad Software Inc.). The Student *t*-test was used for two-group comparisons. The values $*P < 0.05$, $**P < 0.01$, $***P < 0.001$, and $****P < 0.001$ were considered significant. n.s. stands for not significant.

Extended data figure legends

Extended data fig. 1: SARS-CoV-2 induced syncytia formation

a Representative immunofluorescence images of SARS-CoV-2-induced syncytia. HeLa-ACE2 cells stably expressing mCherry (HeLa-ACE2-mCherry) were infected with SARS-CoV-2 at an MOI of 0.5. After 18 h, cells were fixed and stained with DAPI (blue) and anti-NP antibody (green). Scale bar, 250 μm. **b** Syncytia formation ratio at different time points post SARS-CoV-2 infection. HeLa-ACE2-mCherry cells were infected with SARS-CoV-2 at an MOI of 0.5 for indicated times. Syncytia formation ratios were calculated by dividing mCherry positive cells containing more than two or three nuclei by total mCherry positive cells using a high content imaging instrument. **c** Representative immunofluorescence images of SARS-CoV-2-induced syncytia in Calu-3 (upper) and THP-1 macrophage cells (lower). Calu-3 cells or macrophage-like cells differentiated from THP-1 cells using phorbol-12-myristate-13-acetate (PMA) were infected with SARS-CoV-2 at an

MOI of 0.5. After 18 h, cells were fixed and stained with DAPI (blue) and anti-NP antibody (green). Scale bar, 40 μm. **d** Representative immunofluorescence images of SARS-CoV-2-infected cells stained with anti-NP antibody (green), anti-Lamin B1 antibody (red), and DAPI (blue). HeLa-ACE2 cells were infected as indicated in (**a**), Scale bar, 40 μm. **e** Representative images of cells stained with anti-NP antibody (green), DAPI (blue), anti-cGAS antibody (red). cGAS-null HeLa-ACE2 cells reconstituted with cGAS-Flag were infected with SARS-CoV-2 at an MOI of 0.5 for 18 h, followed by staining as indicated. Scale bar, 40 μm.

Extended data fig. 2: Activation of innate immune response by cell co-culture

a Scheme of co-culture experiment. **b** Representative fluorescence images of co-culture experiment. HEK293T cells were transfected with vector control (Vec) or increasing amounts of plasmids expressing EGFP and spike. After 24 h, cells were detached and mixed with wild-type HeLa for 8 h. Cells were then subjected to fluorescence microscopy analysis. Scale bar, 250 μm. **c** Cytokine genes/ISGs expression in co-cultured cells. Cells were co-cultured as indicated in (**b**). RNA extracted from the cells was evaluated by quantitative PCR. The data are expressed as fold change of the *IFNB*, *ISG15*, *IL8*, and *CCL5* mRNA levels relative to the *GAPDH* control. Mean ± s.d., n = 3. n.s., not significant. two-tailed Student's *t*-test. **d** Western blot analysis of cells from co-culture experiment as described in (**b**) using indicated antibodies. **e** cGAS expression level in Hela-ACE2, HeLa-cGAS^{KO}-ACE2, and HeLa-cGAS^{RE}-ACE2 cells. **f** HEK293T cells were transfected with vector control (Vec) or plasmids expressing S. After 24 h, cells were detached and mixed with HeLa-ACE2-mCherry cells (wild-type, cGAS^{KO}, or cGAS^{RE}) for 8 h. Cells were then subjected to fluorescence microscopy analysis. Scale bar, 250 μm. **g** STING expression level in Hela-STING^{KO}-ACE2 cells. **h** MAVS expression level in HeLa-MAVS^{KO}-ACE2 cells.

Extended data fig. 3 cGAS is colocalized with γ-H2AX in syncytial cells

Co-culture experiments were performed as described in Fig. 4e. Cells were stained with DAPI (blue), anti-HA (red) antibody, and anti-γ-H2AX (green) antibody. Three-dimensional reconstructed images were displayed as orthoslice view. Scale bar, 20 μm or (inset) 5 μm.

Extended data fig. 4 The antiviral effect of Remdesivir on SARS-CoV-2

a, **b** Cells were treated with serially diluted Remdesivir for 24 h (Calu-3) or 1 h (HeLa-ACE2). Cells were then subjected to viability assay or infected with SARS-CoV-2 at an MOI of 0.2. After 24 h (Calu-3) or 48 h (HeLa-ACE2), supernatants were harvested for RNA extraction, followed by absolute quantification of viral *N* mRNA by PCR. The IC_{50} (The half-maximal inhibitory concentration) and CC_{50} (The half-maximal cytotoxic concentration) values were calculated using Prism software.

Acknowledgments

This work was supported by grants from National Key R&D Program of China (2020YFA0707600 to Z.Z., 2020YFA0707800 to W.W.), the National Major Sciences & Technology Project for Control and Prevention of Major Infectious Diseases in China (2018ZX10301401 to Z.Z. and X.L.), the National Natural Science Foundation of China (81930063, 31870893, and 81971948 to J.W., Z. Z, and X.L.), the Beijing Municipal Science & Technology Commission (Z181100001318009), Chinese Academy of Medical Sciences (CAMS) Innovation Fund for Medical Sciences (2016-I2M-1-014, 2016-I2M-1-005 to J.W. and X.L.), the Beijing Advanced Innovation Center for Genomics (ICG) at Peking University, and the Peking-Tsinghua Center for Life Sciences.

We thank the Imaging Core and Flow Cytometry Core at National Center for Protein Sciences at Peking University, particularly Liqin Fu and Huan Yang, for technical help. We thank the imaging facility at the Center for Quantitative Biology at Peking University, particularly Xin Li, for assistance with confocal microscopy.

Author contributions

Project conception: Z.Z., Z.D., and J.W.; Experimental design: Z.Z., X.Z., X.L., X.X., Z.D., W.W., and J.W.; Experimental work: X.Z., X.X., Z.Z., X.L., R.M., X.D., Q.J., W.W., T. J., Y.S., T.Z.; Data analysis: Z.Z., X.Z., X.L., Y.T., Z.X., Z.D., W.W., L.R., and J.W.; Writing original draft: Z.Z. and J.W.; Writing review and editing, Z.D., J.W., W.W., Z.Z., X.Z., X.L., T.D., and Z.J.; All authors reviewed the manuscript.

Competing interests

The authors declare no competing interests.

1 Ren, L. L. *et al.* Identification of a novel coronavirus causing severe pneumonia in human: a descriptive study. *Chin Med J (Engl)*, doi:10.1097/CM9.0000000000000722 (2020).

2 Huang, C. *et al.* Clinical features of patients infected with 2019 novel coronavirus in Wuhan, China. *Lancet* **395**, 497-506, doi:10.1016/S0140-6736(20)30183-5 (2020).

3 Akira, S., Uematsu, S. & Takeuchi, O. Pathogen recognition and innate immunity. *Cell* **124**, 783-801, doi:10.1016/j.cell.2006.02.015 (2006).

4 Schlee, M. & Hartmann, G. Discriminating self from non-self in nucleic acid sensing. *Nat Rev Immunol* **16**, 566-580, doi:10.1038/nri.2016.78 (2016).

5 Crowl, J. T., Gray, E. E., Pestal, K., Volkman, H. E. & Stetson, D. B. Intracellular Nucleic Acid Detection in Autoimmunity. *Annu Rev Immunol* **35**, 313-336, doi:10.1146/annurev-immunol-051116-052331 (2017).

6 Lei, X. *et al.* Activation and evasion of type I interferon responses by SARS-CoV-2. *Nat Commun* **11**, 3810, doi:10.1038/s41467-020-17665-9 (2020).

7 Miorin, L. *et al.* SARS-CoV-2 Orf6 hijacks Nup98 to block STAT nuclear import and antagonize interferon signaling. *Proc Natl Acad Sci U S A* **117**, 28344-28354, doi:10.1073/pnas.2016650117 (2020).

8 Xia, H. *et al.* Evasion of Type I Interferon by SARS-CoV-2. *Cell Rep* **33**, 108234, doi:10.1016/j.celrep.2020.108234 (2020).

9 Fu, Y. Z. *et al.* SARS-CoV-2 membrane glycoprotein M antagonizes the MAVS-mediated innate antiviral response. *Cell Mol Immunol*, doi:10.1038/s41423-020-00571-x (2020).

10 Liu, G. *et al.* ISG15-dependent Activation of the RNA Sensor MDA5 and its Antagonism by the SARS-CoV-2 papain-like protease. 2020.2010.2026.356048, doi:10.1101/2020.10.26.356048 %J bioRxiv (2020).

11 Hadjadj, J. *et al.* Impaired type I interferon activity and inflammatory responses in severe COVID-19 patients. *Science* **369**, 718-724, doi:10.1126/science.abc6027 (2020).

12 Winkler, E. S. *et al.* SARS-CoV-2 infection of human ACE2-transgenic mice causes severe lung inflammation and impaired function. *Nat Immunol* **21**, 1327-1335, doi:10.1038/s41590-020-0778-2 (2020).

13 Israelow, B. *et al.* Mouse model of SARS-CoV-2 reveals inflammatory role of type I interferon signaling. *J Exp Med* **217**, doi:10.1084/jem.20201241 (2020).

14 Zhou, Z. *et al.* Heightened Innate Immune Responses in the Respiratory Tract of COVID-19 Patients. *Cell Host Microbe* **27**, 883-890 e882, doi:10.1016/j.chom.2020.04.017 (2020).

15 Lucas, C. *et al.* Longitudinal analyses reveal immunological misfiring in severe COVID-19. *Nature* **584**, 463-469, doi:10.1038/s41586-020-2588-y (2020).

16 Broggi, A. *et al.* Type III interferons disrupt the lung epithelial barrier upon viral recognition. *Science* **369**, 706-712, doi:10.1126/science.abc3545 (2020).

17 Lee, J. S. *et al.* Immunophenotyping of COVID-19 and influenza highlights the role of type I interferons in development of severe COVID-19. *Sci Immunol* **5**, doi:10.1126/sciimmunol.abd1554 (2020).

18 Wilk, A. J. *et al.* A single-cell atlas of the peripheral immune response in patients with severe COVID-19. *Nat Med* **26**, 1070-1076, doi:10.1038/s41591-020-0944-y (2020).

19 Buchrieser, J. *et al.* Syncytia formation by SARS-CoV-2-infected cells. *EMBO J* **39**, e106267, doi:10.15252/embj.2020106267 (2020).

20 Zhu, N. *et al.* Morphogenesis and cytopathic effect of SARS-CoV-2 infection in human airway epithelial cells. *Nat Commun* **11**, 3910, doi:10.1038/s41467-020-17796-z (2020).

21 Rockx, B. *et al.* Comparative pathogenesis of COVID-19, MERS, and SARS in a nonhuman primate model. *Science* **368**, 1012-1015, doi:10.1126/science.abb7314 (2020).

22 Xu, Z. *et al.* Pathological findings of COVID-19 associated with acute respiratory distress syndrome. *Lancet Respir Med* **8**, 420-422, doi:10.1016/S2213-2600(20)30076-X (2020).

23 Liu, S. *et al.* Phosphorylation of innate immune adaptor proteins MAVS, STING, and TRIF induces IRF3 activation. *Science* **347**, aaa2630, doi:10.1126/science.aaa2630 (2015).

24 Haag, S. M. *et al.* Targeting STING with covalent small-molecule inhibitors. *Nature* **559**, 269-273, doi:10.1038/s41586-018-0287-8 (2018).

25 Mackenzie, K. J. *et al.* cGAS surveillance of micronuclei links genome instability to innate immunity. *Nature* **548**, 461-465, doi:10.1038/nature23449 (2017).

26 Harding, S. M. *et al.* Mitotic progression following DNA damage enables pattern recognition within micronuclei. *Nature* **548**, 466-470, doi:10.1038/nature23470 (2017).

27 Gluck, S. *et al.* Innate immune sensing of cytosolic chromatin fragments through cGAS promotes senescence. *Nat Cell Biol* **19**, 1061-1070, doi:10.1038/ncb3586 (2017).

28 Dou, Z. *et al.* Cytoplasmic chromatin triggers inflammation in senescence and cancer. *Nature* **550**, 402-406, doi:10.1038/nature24050 (2017).

29 Tiku, V., Tan, M. W. & Dikic, I. Mitochondrial Functions in Infection and Immunity. *Trends Cell Biol* **30**, 263-275, doi:10.1016/j.tcb.2020.01.006 (2020).

30 Hoffmann, M. *et al.* SARS-CoV-2 Cell Entry Depends on ACE2 and TMPRSS2 and Is Blocked by a Clinically Proven Protease Inhibitor. *Cell* **181**, 271-280 e278, doi:10.1016/j.cell.2020.02.052 (2020).

31 Ivanov, A. *et al.* Lysosome-mediated processing of chromatin in senescence. *J Cell Biol* **202**, 129-143, doi:10.1083/jcb.201212110 (2013).

32 Yang, H., Wang, H., Ren, J., Chen, Q. & Chen, Z. J. cGAS is essential for cellular senescence. *Proc Natl Acad Sci U S A* **114**, E4612-E4620, doi:10.1073/pnas.1705499114 (2017).

33 Li, T. & Chen, Z. J. The cGAS-cGAMP-STING pathway connects DNA damage to inflammation, senescence, and cancer. *J Exp Med* **215**, 1287-1299, doi:10.1084/jem.20180139 (2018).

34 Ablasser, A. & Chen, Z. J. cGAS in action: Expanding roles in immunity and inflammation. *Science* **363**, doi:10.1126/science.aat8657 (2019).

35 Yum, S., Li, M., Frankel, A. E. & Chen, Z. J. Roles of the cGAS-STING Pathway in Cancer Immunosurveillance and Immunotherapy. **3**, 323-344, doi:10.1146/annurev-cancerbio-030518-055636 (2019).

36 Ramanjulu, J. M. *et al.* Design of amidobenzimidazole STING receptor agonists with systemic activity. *Nature* **564**, 439-443, doi:10.1038/s41586-018-0705-y (2018).

37 Frankel, S. S. *et al.* Replication of HIV-1 in dendritic cell-derived syncytia at the mucosal surface of the adenoid. *Science* **272**, 115-117, doi:10.1126/science.272.5258.115 (1996).

38 White, J., Matlin, K. & Helenius, A. Cell fusion by Semliki Forest, influenza, and vesicular stomatitis viruses. *J Cell Biol* **89**, 674-679, doi:10.1083/jcb.89.3.674 (1981).

39 Oren-Suissa, M. & Podbilewicz, B. Cell fusion during development. *Trends Cell Biol* **17**, 537-

546, doi:10.1016/j.tcb.2007.09.004 (2007).

40 Lu, X. & Kang, Y. Cell fusion as a hidden force in tumor progression. *Cancer Res* **69**, 8536-8539, doi:10.1158/0008-5472.CAN-09-2159 (2009).

41 Chuprin, A. *et al.* Cell fusion induced by ERVWE1 or measles virus causes cellular senescence. *Genes Dev* **27**, 2356-2366, doi:10.1101/gad.227512.113 (2013).

42 Park, A. & Iwasaki, A. Type I and Type III Interferons - Induction, Signaling, Evasion, and Application to Combat COVID-19. *Cell Host Microbe* **27**, 870-878, doi:10.1016/j.chom.2020.05.008 (2020).

43 Franz, K. M., Neidermyer, W. J., Tan, Y. J., Whelan, S. P. J. & Kagan, J. C. STING-dependent translation inhibition restricts RNA virus replication. *Proc Natl Acad Sci U S A* **115**, E2058-E2067, doi:10.1073/pnas.1716937115 (2018).

44 Zhu, Q. *et al.* A synthetic STING agonist inhibits the replication of human parainfluenza virus 3 and rhinovirus 16 through distinct mechanisms. *Antiviral Res* **183**, 104933, doi:10.1016/j.antiviral.2020.104933 (2020).

45 Vizioli, M. G. *et al.* Mitochondria-to-nucleus retrograde signaling drives formation of cytoplasmic chromatin and inflammation in senescence. *Genes Dev* **34**, 428-445, doi:10.1101/gad.331272.119 (2020).

46 Bussani, R. *et al.* Persistence of viral RNA, pneumocyte syncytia and thrombosis are hallmarks of advanced COVID-19 pathology. *EBioMedicine* **61**, 103104, doi:10.1016/j.ebiom.2020.103104 (2020).

47 Wang, C. *et al.* Manganese Increases the Sensitivity of the cGAS-STING Pathway for Double-Stranded DNA and Is Required for the Host Defense against DNA Viruses. *Immunity* **48**, 675-687 e677, doi:10.1016/j.immuni.2018.03.017 (2018).

48 Wang, Y. *et al.* Inflammasome Activation Triggers Caspase-1-Mediated Cleavage of cGAS to Regulate Responses to DNA Virus Infection. *Immunity* **46**, 393-404, doi:10.1016/j.immuni.2017.02.011 (2017).

Fig. 1

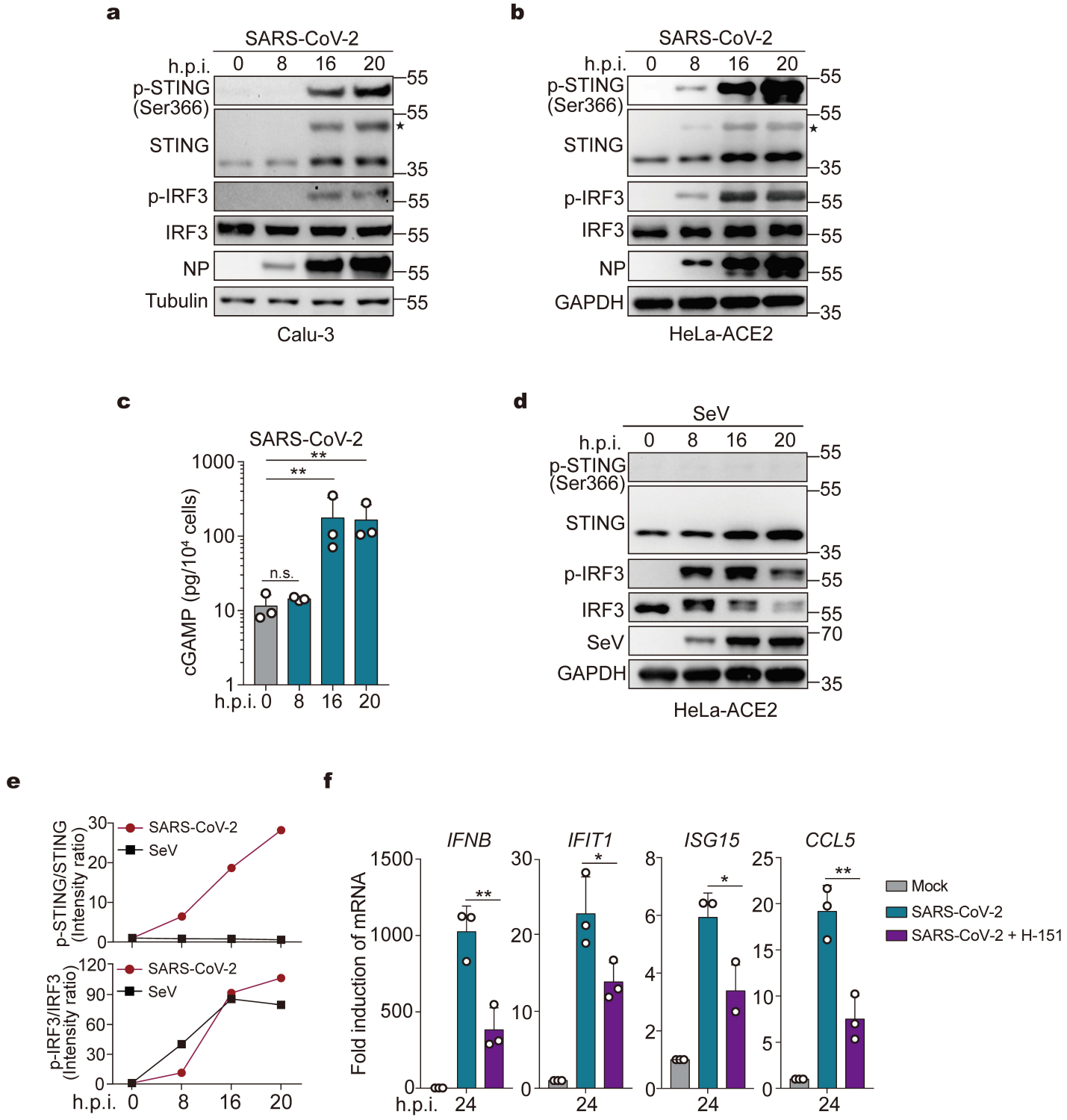
a
SARS-CoV-2
h.p.i. 0 8 16 20
p-STING (Ser366)
STING
p-IRF3
IRF3
NP
Tubulin
55
55
35
55
55
55
Calu-3
b
SARS-CoV-2
h.p.i. 0 8 16 20
p-STING (Ser366)
STING
p-IRF3
IRF3
NP
GAPDH
55
55
35
55
55
35
HeLa-ACE2
c
SARS-CoV-2
cGAMP (pg/10⁴ cells)
1000
100
10
1
n.s.
**
**
h.p.i. 0 8 16 20
d
SeV
h.p.i. 0 8 16 20
p-STING (Ser366)
STING
p-IRF3
IRF3
SeV
GAPDH
55
55
35
55
55
70
35
HeLa-ACE2
e
p-STING/STING (Intensity ratio)
SARS-CoV-2
SeV
p-IRF3/IRF3 (Intensity ratio)
h.p.i. 0 8 16 20
f
IFNB
IFIT1
ISG15
CCL5
Fold induction of mRNA
h.p.i. 24
Mock
SARS-CoV-2
SARS-CoV-2 + H-151

Fig. 2

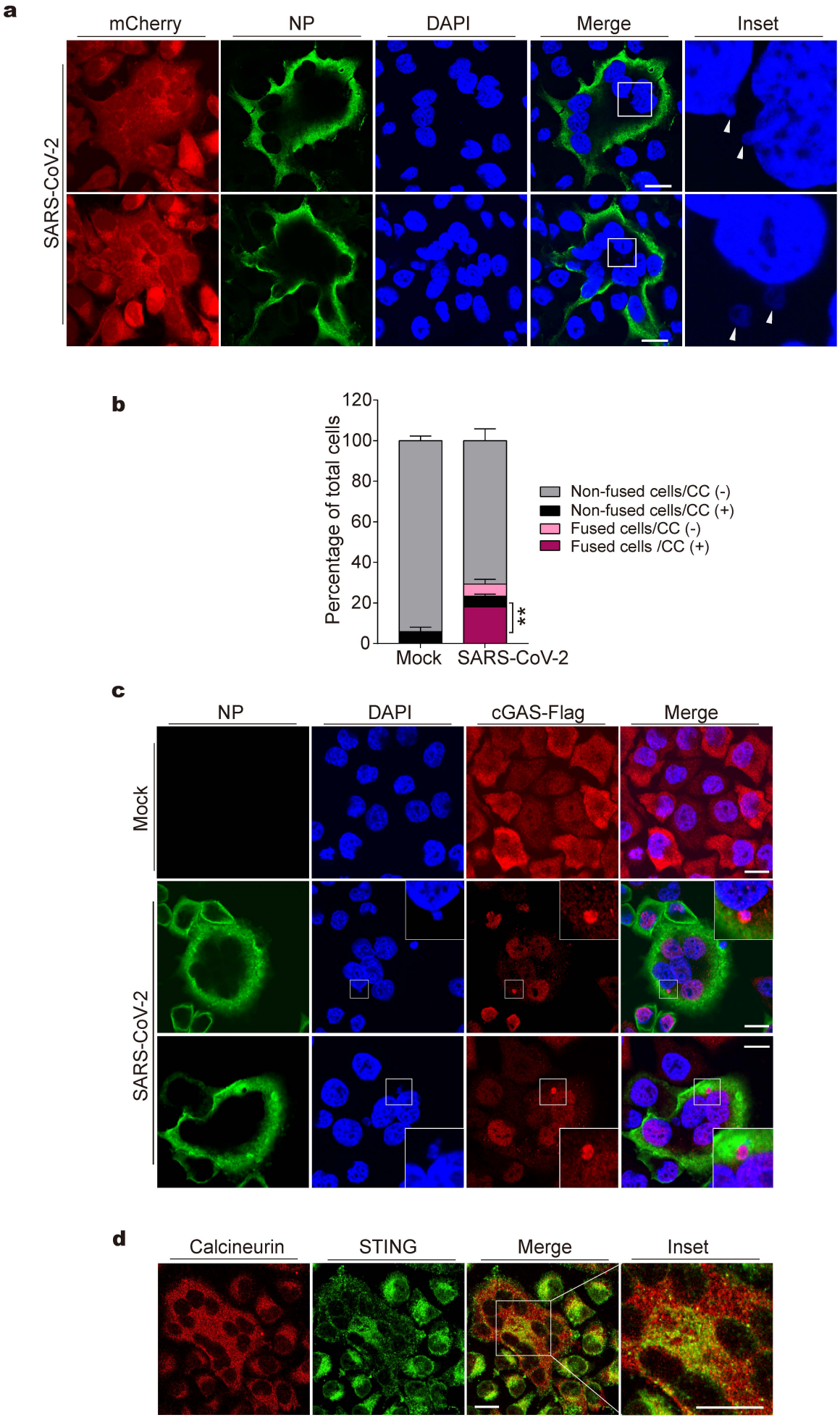
a
mCherry
NP
DAPI
Merge
Inset
SARS-CoV-2
b
Percentage of total cells
120
100
80
60
40
20
0
Mock
SARS-CoV-2
**
Non-fused cells/CC (-)
Non-fused cells/CC (+)
Fused cells/CC (-)
Fused cells /CC (+)
c
NP
DAPI
cGAS-Flag
Merge
Mock
SARS-CoV-2
d
Calcineurin
STING
Merge
Inset

Fig. 3

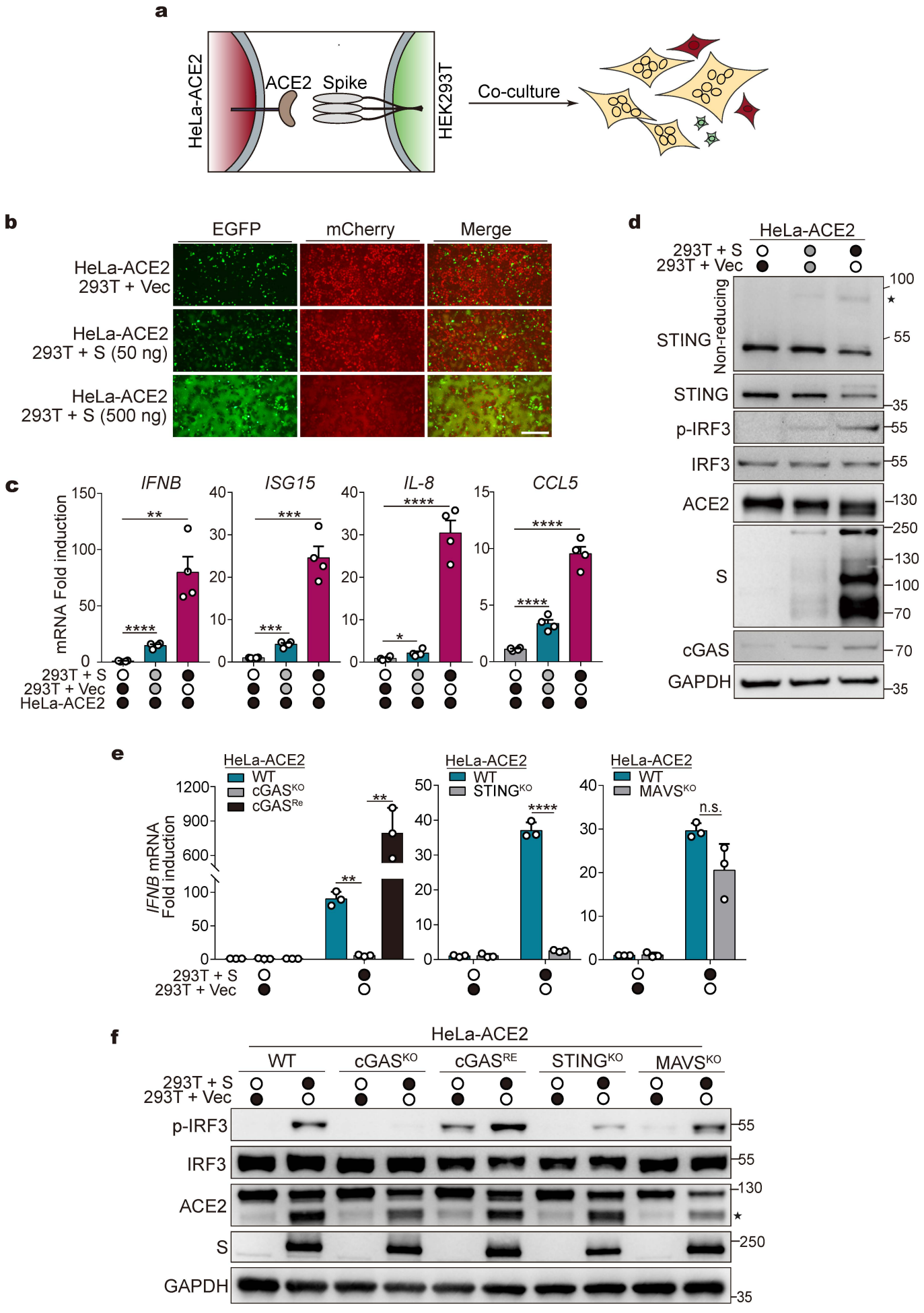
a
HeLa-ACE2
ACE2
Spike
HEK293T
Co-culture
b
EGFP
mCherry
Merge
HeLa-ACE2
293T + Vec
HeLa-ACE2
293T + S (50 ng)
HeLa-ACE2
293T + S (500 ng)
c
IFNB
ISG15
IL-8
CCL5
mRNA Fold induction
293T + S
293T + Vec
HeLa-ACE2
d
HeLa-ACE2
293T + S
293T + Vec
STING
Non-reducing
STING
p-IRF3
IRF3
ACE2
S
cGAS
GAPDH
e
HeLa-ACE2
WT
cGASKO
cGASRe
STINGKO
MAVSKO
IFNB mRNA
Fold induction
n.s.
293T + S
293T + Vec
f
HeLa-ACE2
WT
cGASKO
cGASRE
STINGKO
MAVSKO
293T + S
293T + Vec
p-IRF3
IRF3
ACE2
S
GAPDH

Fig. 4

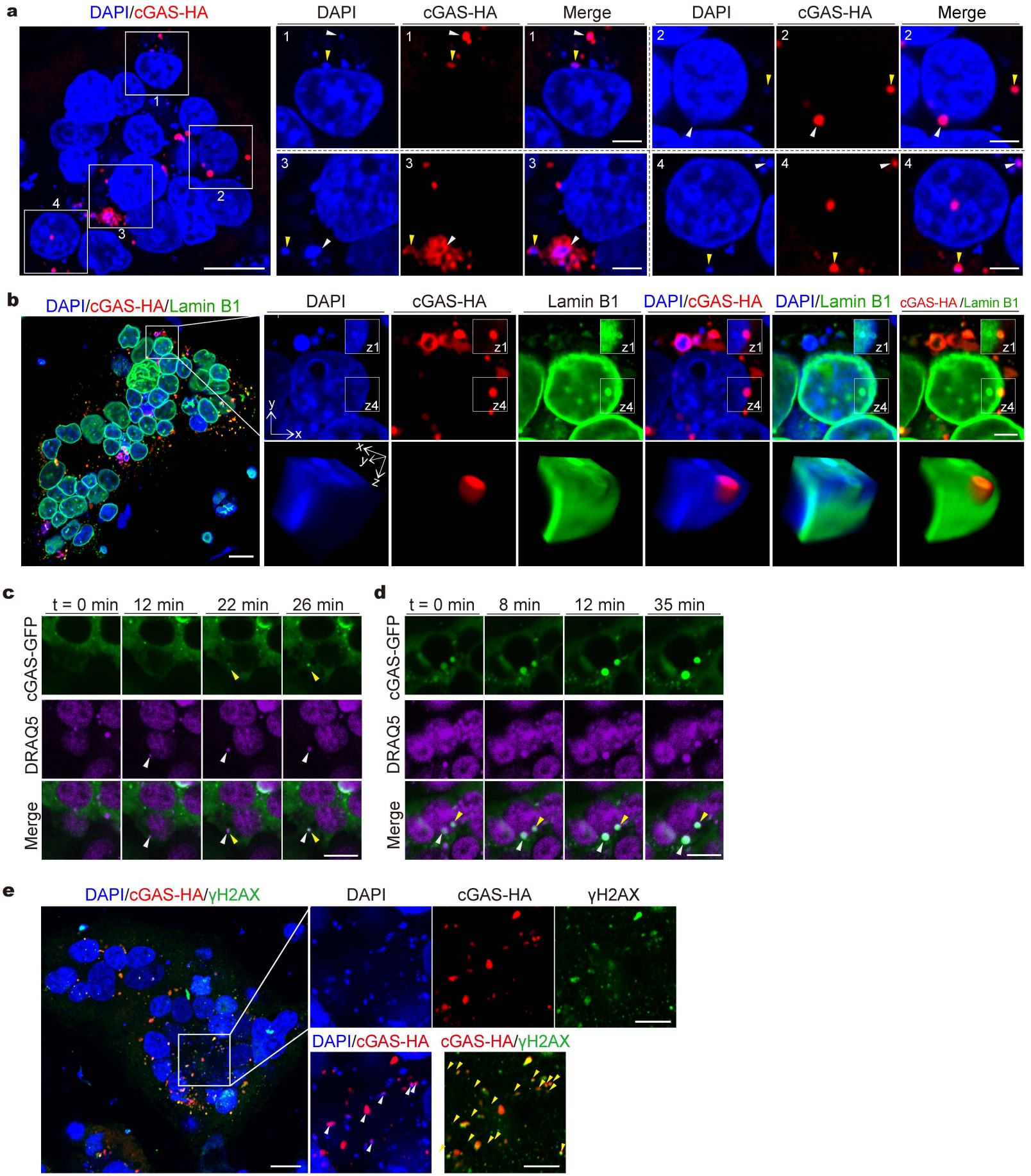
a
DAPI/cGAS-HA
DAPI
cGAS-HA
Merge
b
DAPI/cGAS-HA/Lamin B1
Lamin B1
DAPI/Lamin B1
cGAS-HA /Lamin B1
c
t = 0 min
12 min
22 min
26 min
cGAS-GFP
DRAQ5
Merge
d
8 min
35 min
e
DAPI/cGAS-HA/γH2AX
γH2AX
DAPI/cGAS-HA
cGAS-HA/γH2AX

Fig. 5

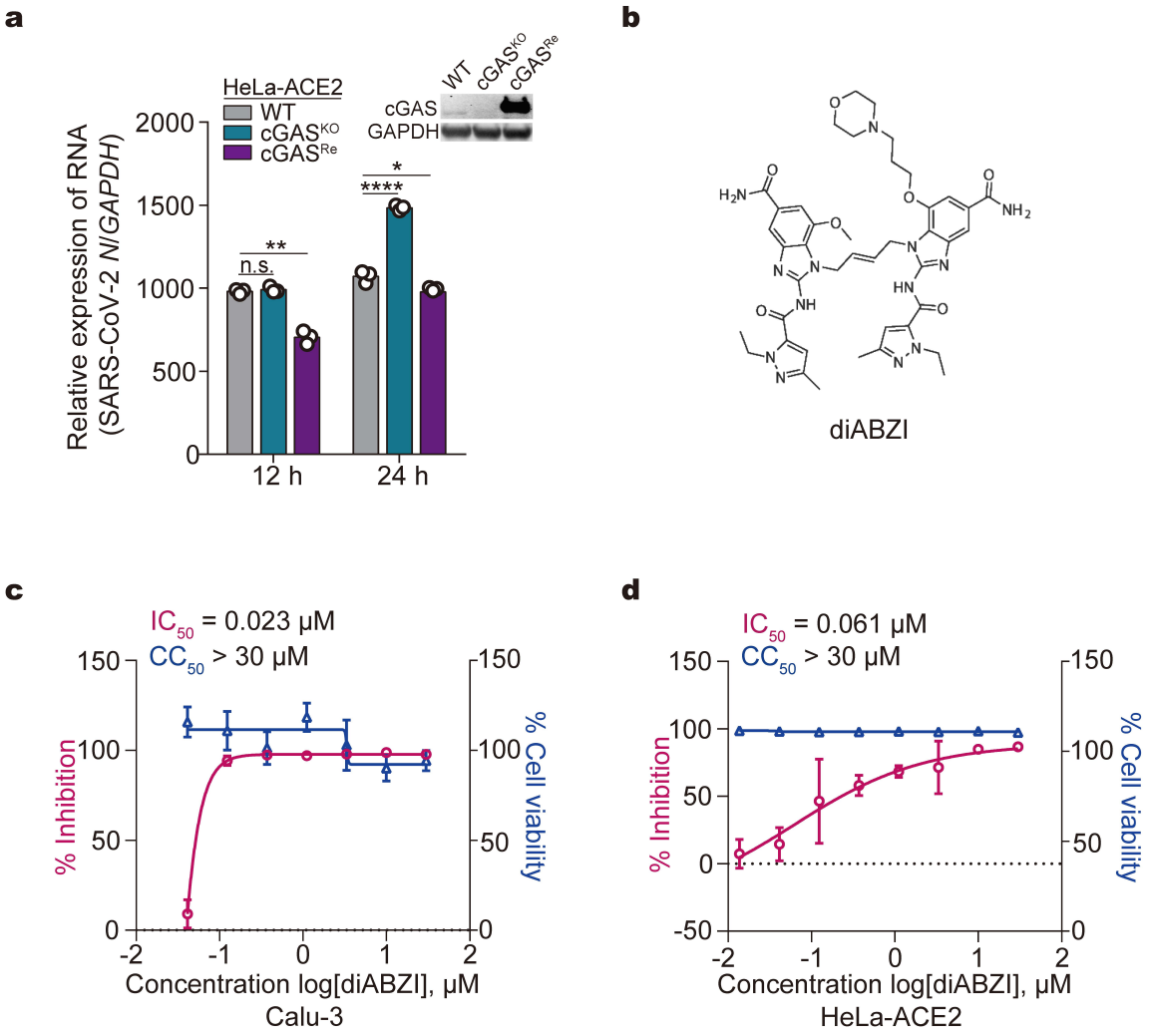
a
HeLa-ACE2
WT
cGAS^KO
cGAS^Re
Relative expression of RNA
(SARS-CoV-2 N/GAPDH)
2000
1500
1000
500
0
n.s.
**
*
****
12 h
24 h
WT
cGAS^KO
cGAS^Re
cGAS
GAPDH
b
diABZI
c
IC50 = 0.023 μM
CC50 > 30 μM
% Inhibition
% Cell viability
Concentration log[diABZI], μM
Calu-3
d
IC50 = 0.061 μM
CC50 > 30 μM
% Inhibition
% Cell viability
Concentration log[diABZI], μM
HeLa-ACE2

Extended Fig. 1

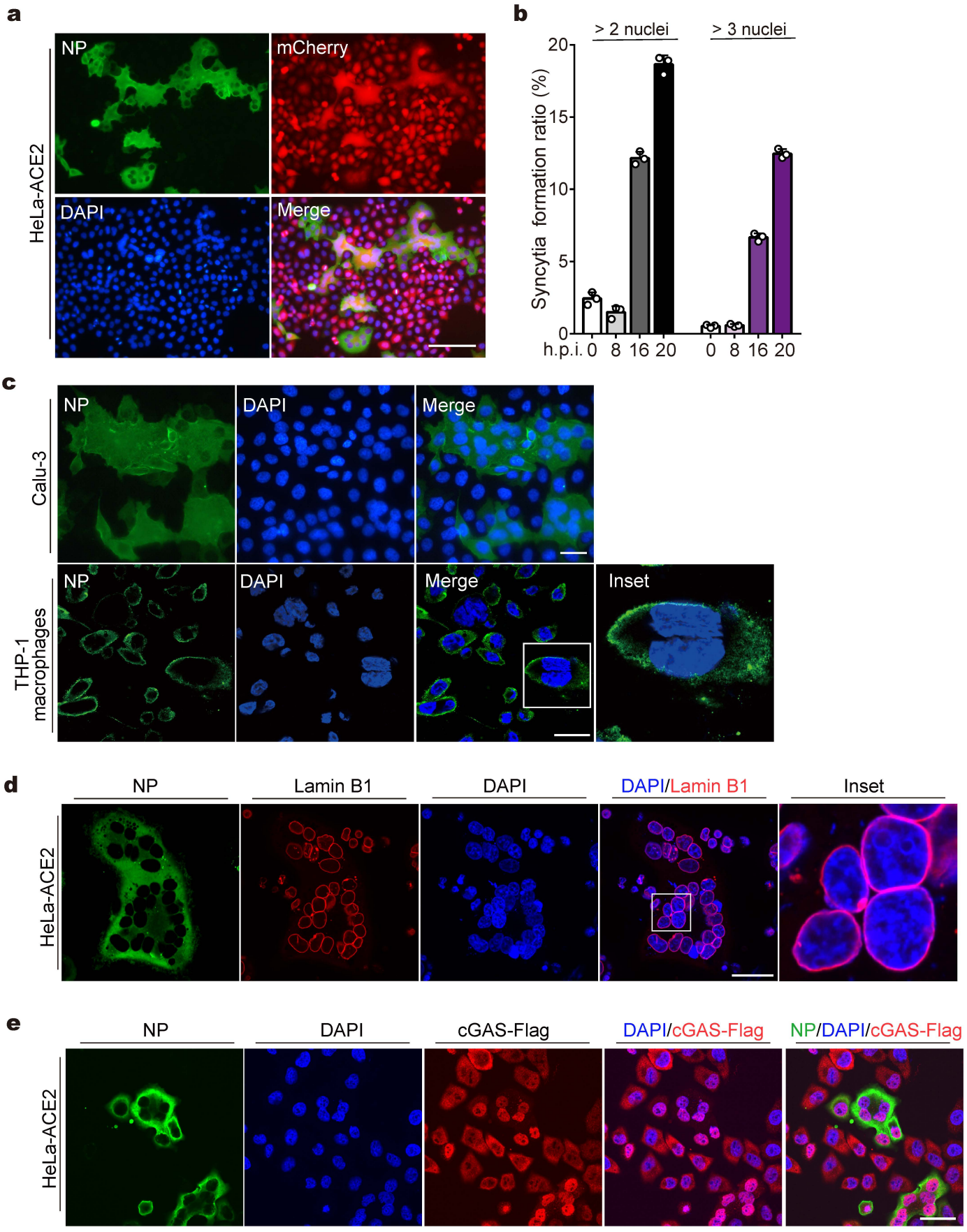

Extended Fig. 2

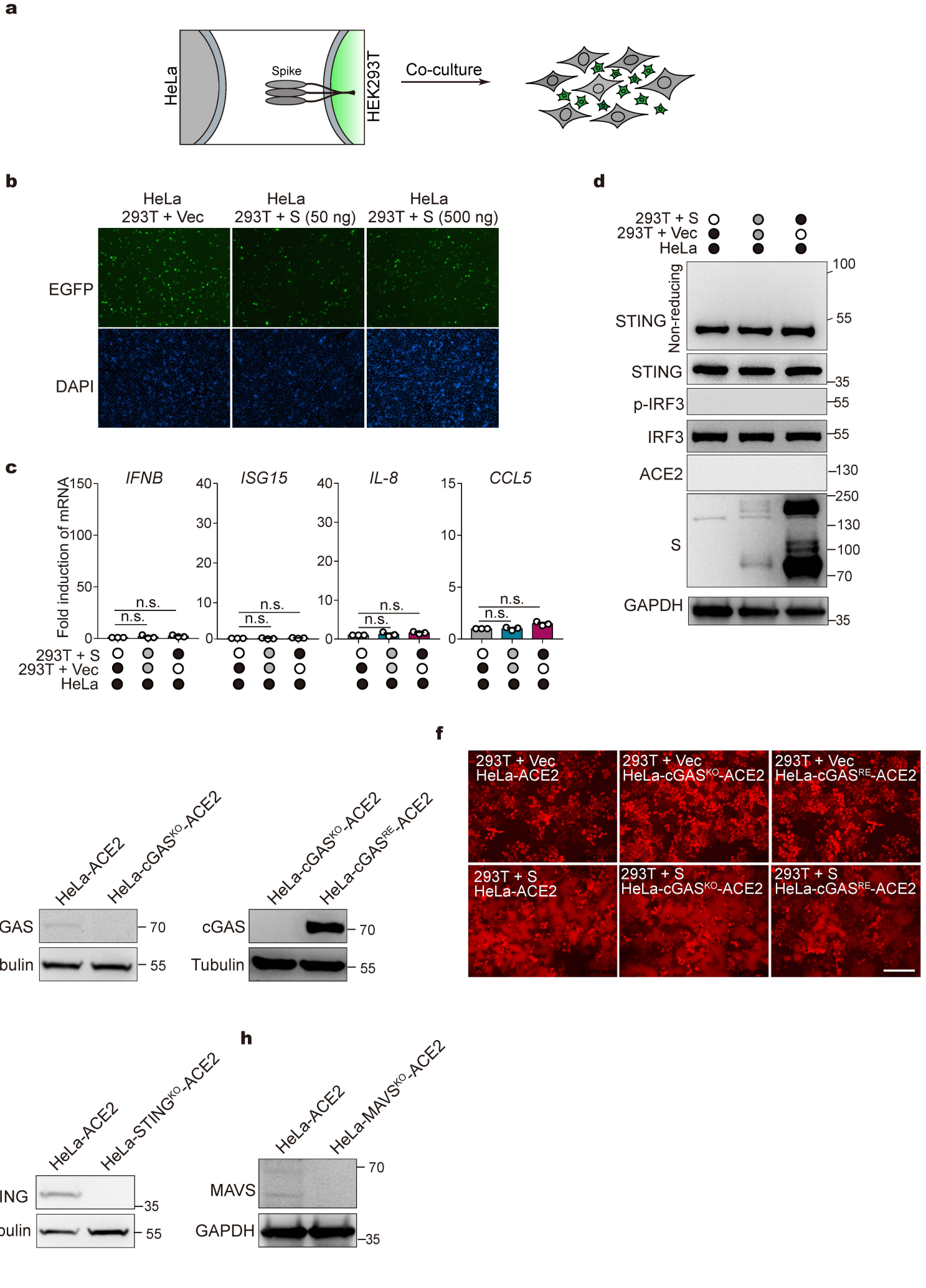

Extended Fig. 3

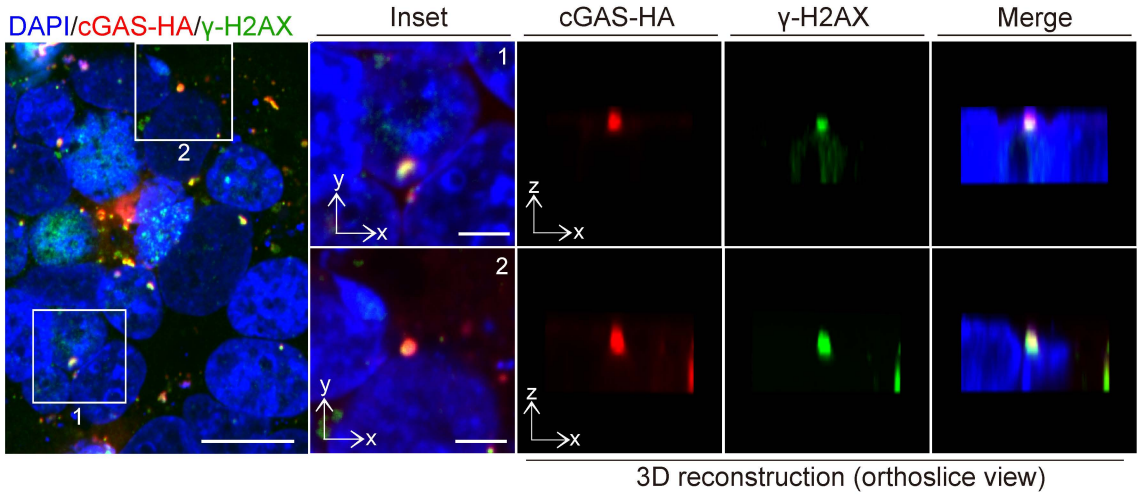

Extended Fig.4

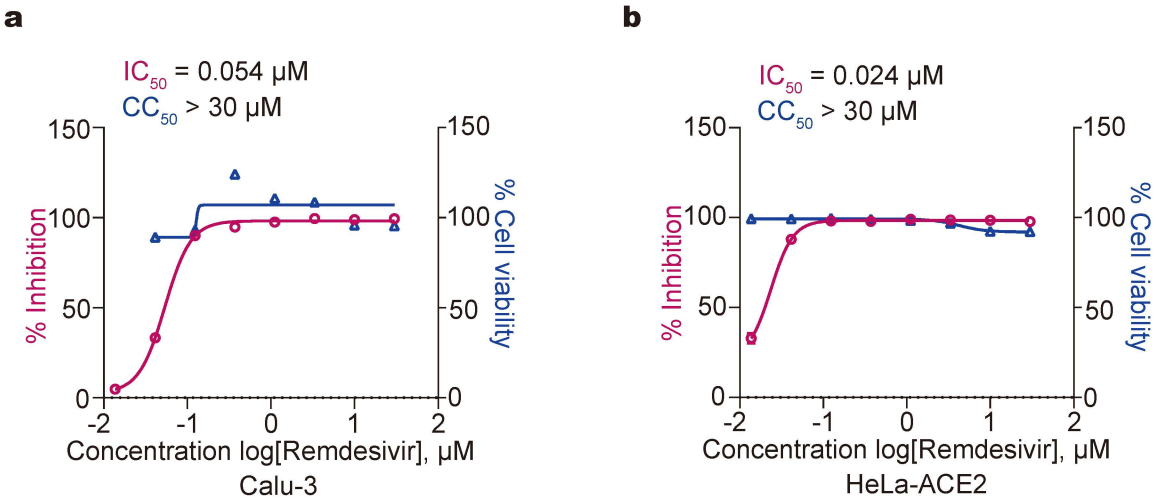

Figures

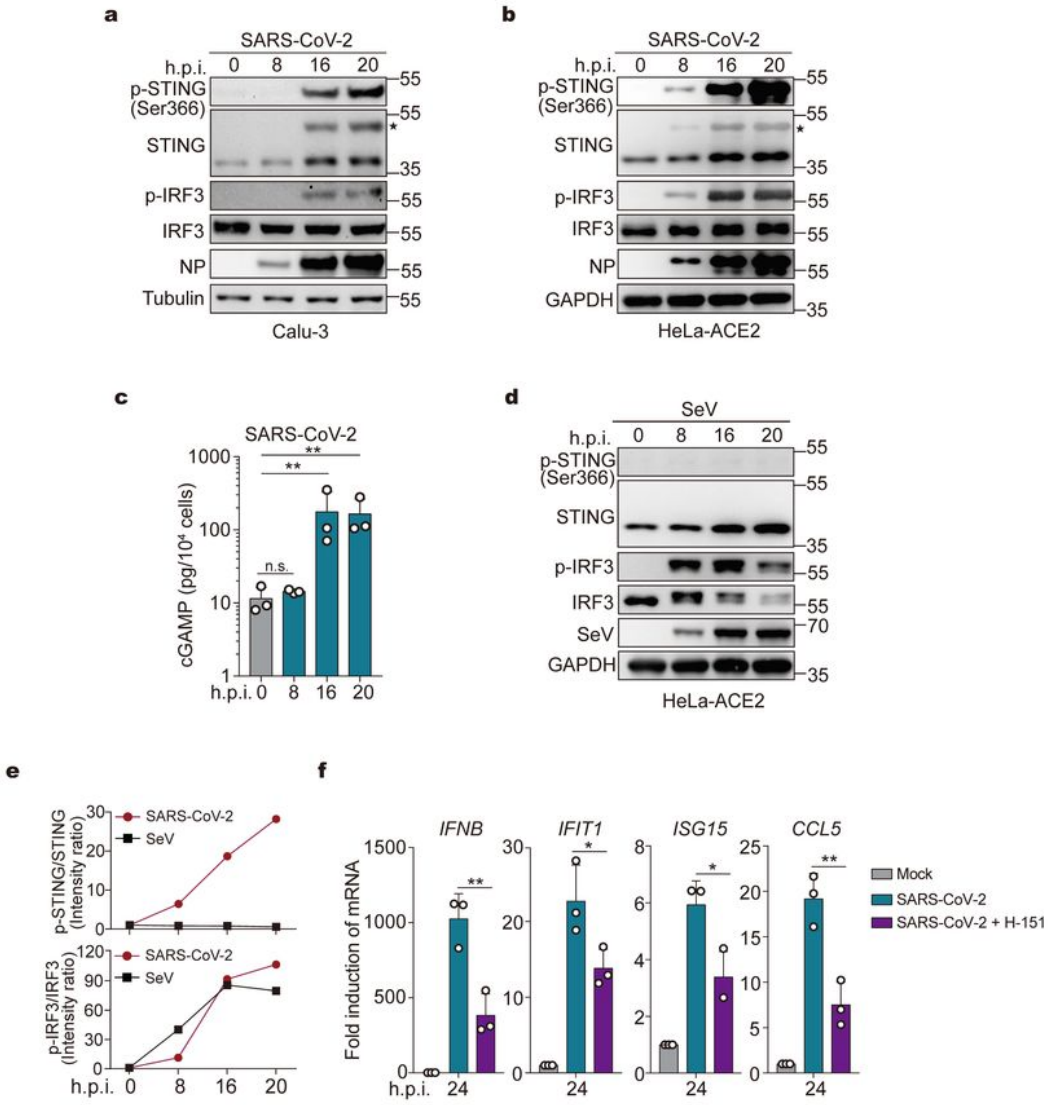

Figure 1

SARS-CoV-2 infection activates the cGAS-STING pathway a, b Representative Western blots of STING and IRF3 phosphorylation upon SARS-CoV-2 infection (n = 2 independent experiments). Calu-3 (a) or HeLa-ACE2 (b) cells were mock-infected or infected with SARS-CoV-2 at an MOI of 0.5. At indicated time points

after infection, cells were harvested and lysed. Lysates were then subjected to Western blot analysis using indicated antibodies. Activated STING. c 2'3'-cGAMP levels in cells infected with SARS-CoV-2. HeLa-ACE2 were infected with SARS-CoV-2 as described in (b). A competitive ELISA assay determined the 2'3'- cGAMP concentrations. Mean ± s.d., n = 3 independent experiments. **P < 0.01, n.s., not significant. Two-tailed Student's t-test on log-transformed data.d STING and IRF3 phosphorylation upon SeV infection. HeLa-ACE2 cells were mock-infected or infected with SeV. Cells were harvested at indicated times and analyzed by Western blot. e Semi-quantitative analysis on Western blot results from (a) and (d) by densitometry. f Calu-3 cells were treated with DMSO or 200 ng/ml of H-151. After 2 h, cells were mock-infected or infected with SARS-CoV-2 at an MOI of 0.5 for 24 h. RNA extracted from the cells was evaluated by quantitative PCR. The data are expressed as fold change of the IFNB, IFIT1, ISG15, and CCL5 mRNA levels relative to the GAPDH control. Mean ± s.d., n = 3 independent experiments. *P < 0.05, **P < 0.01, two-tailed Student's t-test.

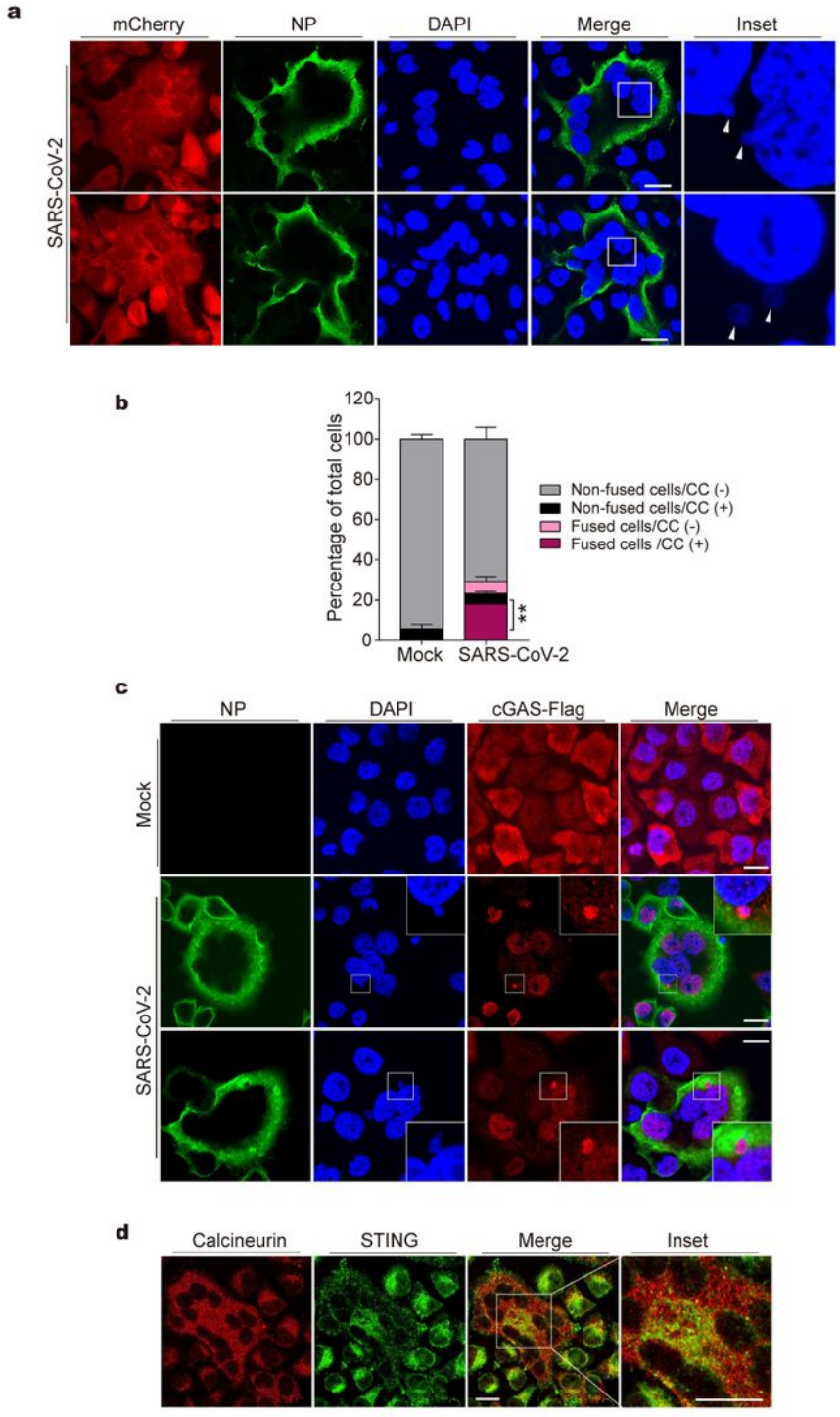

Figure 2

cGAS colocalizes with cytosolic genomic DNA in SARS-CoV-2-induced syncytia a Representative confocal immunofluorescence images of SARS-CoV-2-induced syncytia. HeLa-ACE2 cells stably expressing mCherry were infected with SARS-CoV-2 at an MOI of 0.5. After 18 h, cells were fixed and stained for DNAwith DAPI (blue) and viral nucleocapsid protein (NP) with anti-NP antibody (green). Triangles indicate budding chromatin (upper) or cytosolic chromatin (lower). b Quantification of cells for parameters as

indicated. Cells were quantified for three different fields with 200 cells. Mean ± s.d., n = 3 independent experiments. **P < 0.01, two-tailed Student's t-test. c Representative images of cells stained for NP, DNA, and cGAS-Flag. cGAS-null HeLa-ACE2 cells reconstituted with cGAS-Flag were infected with SARS-CoV-2 at an MOI of 0.5 for 18 h, followed by staining with anti-NP antibody (green), DAPI (blue), and anti-cGAS antibody (red) as indicated. d Representative images of cells stained for ER and STING. HeLa-ACE2 cells were treated as described in (c) and were stained with anti-calcineurin (red) antibody and anti- STING (green) antibody as indicated. Scale bar, 20 μm

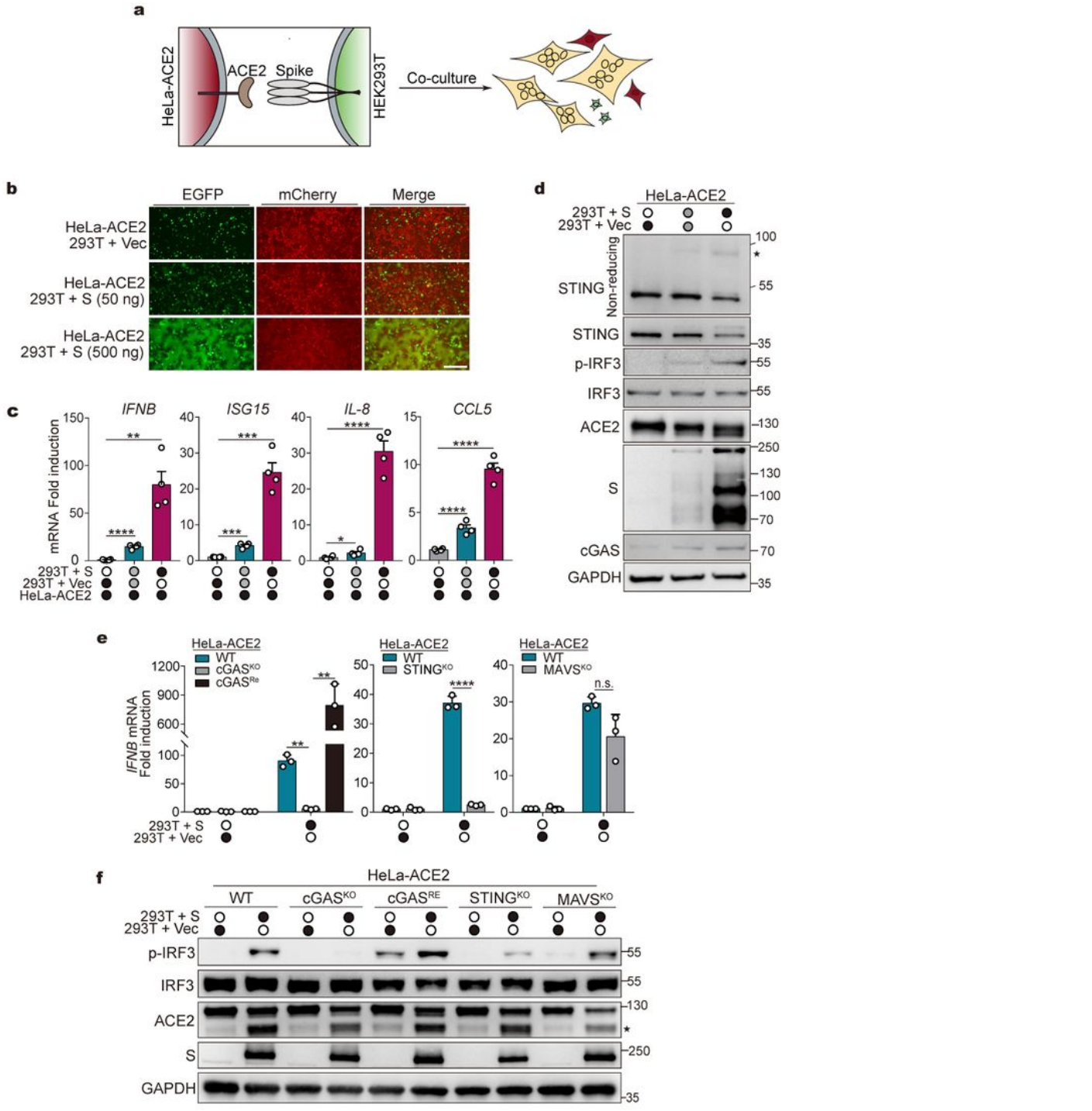

Figure 3

Cell fusion activates the innate immune response via the cGAS-STING pathway a Scheme of co-culture experiment. b Representative fluorescence images of co-culture experiment. HEK293T cells were transfected with vector control (Vec) or increasing amounts of plasmids expressing EGFP and spike for 24 h. Cells were then detached and mixed with HeLa-ACE2 expressing mCherry (HeLa-ACE2-mCherry). After 8 h, cells were subjected to fluorescence microscopy analysis. Scale bar, 250 μm. c Cytokine genes/ISGs expression in co-cultured cells. Cells were co-cultured as indicated in (b). RNA extracted from the cells was evaluated by quantitative PCR. The data are expressed as fold change of the IFNB, ISG15, IL8 and CCL5 mRNA levels relative to the GAPDH control. Mean ± s.d., n = 4 independent experiments. **P < 0.01, ***P < 0.001, ****P < 0.0001, two-tailed Student's t-test. d Western blot analysis of cells from co-culture experiment as described in (b) using indicated antibodies. STING blots were performed under non-reducing (top) or reducing conditions. □ STING dimer. e HEK293T cells were transfected with vector control (Vec) or plasmids expressing spike. After 24 h, cells were detached and mixed with HeLa-ACE2-mCherry cells as indicated. cGASKO, STINGKO, and MAVSKO represent cells depleted of indicated genes. cGASRE represents cGAS-null cells re-expressed cGAS. The expression of IFNB mRNA was assayed as described in (c). Mean ± s.d., n = 3 independent experiments. **P < 0.01, ****P < 0.0001, n.s., not significant. two-tailed Student's t-test. f Western blot analysis of cells from the co-culture experiment as described in (e). □ACE2 fragments generated during cell co-culture. S, Spike.

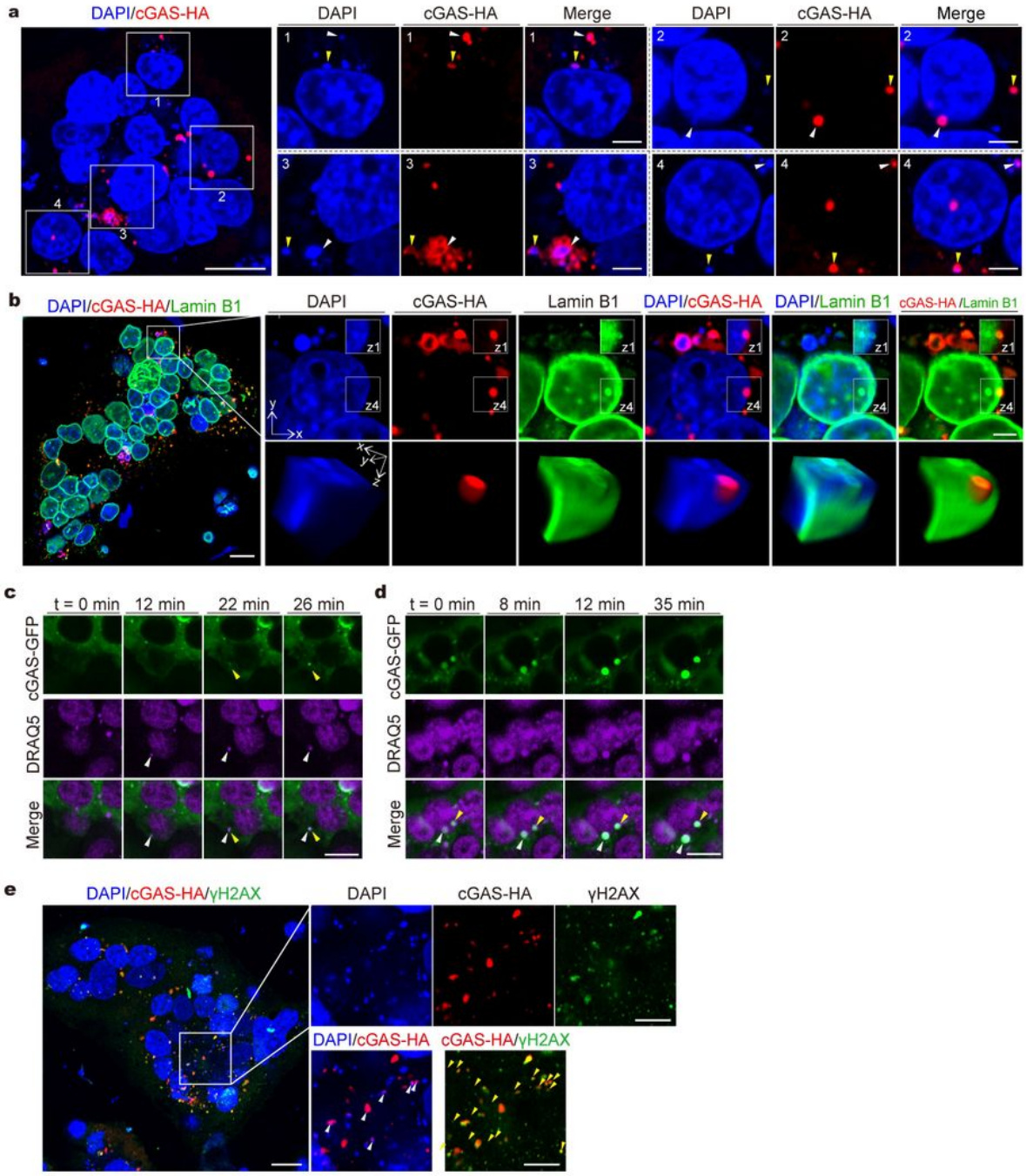

Figure 4

cGAS is colocalized with cytoplasmic chromatin in syncytial cells a Representative confocal immunofluorescence images of co-cultured cells stained for DNA and cGAS-HA. HEK293T cells transfected with plasmids expressing S (HEK293T(S)) were co-cultured with cGAS-null HeLa-ACE2 cells reconstituted with cGAS-HA. After 8 h, cells were stained with DAPI (blue) and anti-HA (red) antibody as indicated. Triangles indicate colocalization of cGAS with cytosolic chromatin. b Representative confocal

immunofluorescence images of co-cultured cells stained for DNA, cGAS-HA, and Lamin B1. Co-culture experiments were performed as described in (a). Cells were stained with DAPI (blue), anti-HA (red), and anti-Lamin B1 (green) antibodies. Three-dimensional reconstructed images based on z-stack images were displayed as volume view. c, d Extracted frames from live-cell imaging of co-cultured cells using Confocal microscopy. HEK293T(S) cells transfected with plasmids expressing cGAS-GFP were co-cultured with cGAS-null HeLa-ACE2 cells transfected with plasmids expressing cGAS-GFP. After 1 h, cells were stained with DRAQ5 (purple) for visualizing DNA and subjected to live -cell imaging. e Coculture experiments were performed as described in (a). Cells were stained with DAPI (blue), anti-HA (red) antibody, and anti-γ-H2AX (green) antibody. Scale bar, 20 μm or (inset) 5 μm.

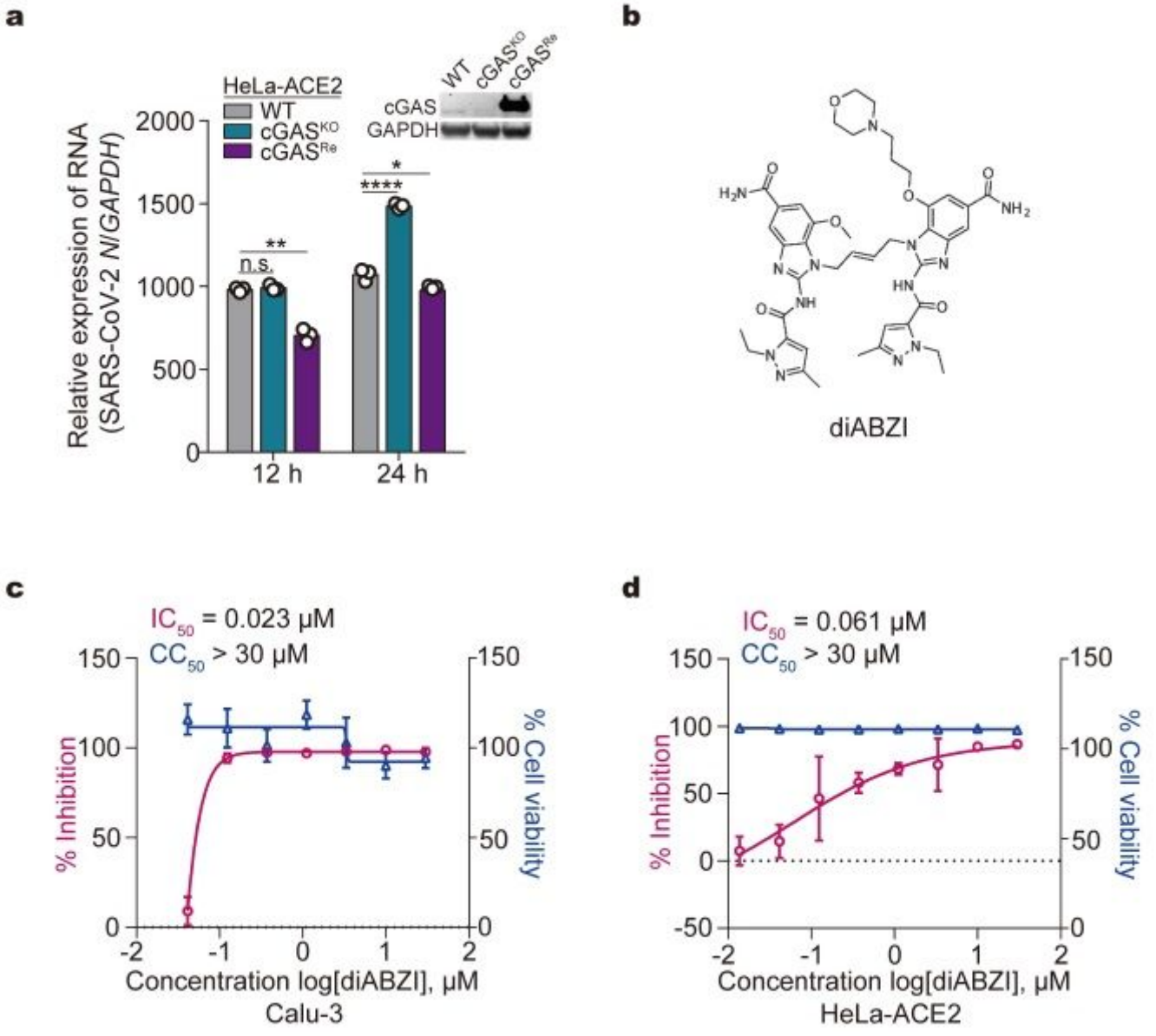

Figure 5

Targeting cGAS-STING pathway as potential therapeutics against SARS-CoV-2 a Effect of cGAS expression on SARS-CoV-2 replication. Wild-type HeLa-ACE2 (WT), HeLacGASKO-ACE2, and HeLa-

cGASRE-ACE2 cells were infected with SARS-CoV-2 at an MOI of 0.5. At indicated times, total RNA extracted from cells was evaluated by quantitative PCR. The data are expressed as fold changes of the RNA levels of the viral N gene relative to the GAPDH control. Mean ± s.d., n = 3. *P < 0.05, **P < 0.01, ****P < 0.0001, n.s., not significant. two-tailed Student's t-test. b The chemical structure of diABZI. c, d Antiviral effect of diABZI on SARS-CoV-2. Calu-3 (c) or HeLa-ACE2 (d) Cells were treated with serially diluted diABZI for 24 h (Calu-3) or 1 h (HeLa-ACE2). Cells were then subjected to viability assay or infected with SARSCoV- 2 at an MOI of 0.2. After 24 h (Calu-3) or 48 h (HeLa-ACE2). Supernatants were harvested for RNA extraction, followed by absolute quantification of viral N mRNA by PCR. Mean ± s.d., n = 4. The IC50 (The half-maximal inhibitory concentration) and CC50 (The halfmaximal cytotoxic concentration) values were calculated using Prism software.

Supplementary Files

This is a list of supplementary files associated with this preprint. Click to download.

- ExtendedDataMovie1.avi
- ExtendedDataMovie2.avi